RESEARCH ARTICLE

Response of a tropical cyclone to a subsurface ocean eddy and the role of boundary layer dynamics

Arjun U. Kumar[1,2] | **Nils Brüggemann[3]** | **Roger K. Smith[4]** | **Jochem Marotzke[1]**

[1]Max Planck Institute for Meteorology, Hamburg, Germany

[2]International Research School on Earth System Modelling, Hamburg, Germany

[3]Faculty of Maths, Informatics and Natural Sciences, University of Hamburg, Hamburg, Germany

[4]Meteorological Institute, Ludwig Maximillian University of Munich, Munich, Germany

Correspondence
A. U. Kumar, Max Planck Institute for Meteorology, Hamburg, Germany.
Email: arjun.kumar@mpimet.mpg.de

Abstract

We analyse a tropical cyclone simulated for a realistic ocean-eddy field using the global, nonhydrostatic, fully coupled atmosphere–ocean ICOsahedral Non-hydrostatic (ICON) model. After intensifying rapidly, the tropical cyclone decays following its interaction with a cold wake and subsequently reintensifies as it encounters a subsurface, warm-core eddy. To understand the change in the azimuthal-mean structure and intensity of the tropical cyclone, we invoke a conceptual framework, which recognises the importance of both boundary-layer dynamics and air–sea interactions. Crucially, the framework recognises that the change in the mean radius of updraught at the boundary-layer top is regulated by the expanding outer tangential wind field through boundary-layer dynamics. The decrease in the average equivalent potential temperature of the boundary-layer updraught during the early decay phase is related to an increase in the mean radius of the updraught rather than air–sea interactions. However, later in the decay phase, air–sea interactions contribute to the decrease, which is accompanied by a decrease in the vertical mass flux in the eyewall updraught and, ultimately, a more pronounced spin-down of the tropical cyclone. Air–sea interactions are also important during reintensification, where the tendencies are reversed, that is, the mean radius of the boundary-layer updraught decreases along with an increase in its average equivalent potential temperature and vertical mass flux. The importance of boundary-layer dynamics to the change in the azimuthal-mean structure is underscored by the ability of a steady-state slab boundary-layer model to predict an increasing and, to a lesser extent, decreasing radius of forced ascent for periods of decay and reintensification, respectively. Finally, our simulation highlights the importance of the ocean-eddy field for tropical cyclone intensity forecasts, since the simulated warm-core eddy does not display any sea-surface temperature (SST) signal until it is encountered by the tropical cyclone.

KEYWORDS

air–sea interactions, boundary-layer dynamics, tropical cyclone intensity, warm-core eddy

1 | INTRODUCTION

This study examines how the atmospheric boundary layer modulates the intensity of a mature tropical cyclone influenced by a realistic ocean-eddy field in a global, convection-permitting, coupled ocean–atmosphere model run at 5-km grid spacing.[1] The significance of the boundary layer to the spin-up and intensity of tropical cyclones is well established for atmosphere-only models (Montgomery and Smith, 2014; 2017). However, two crucial aspects of the boundary layer tested in atmosphere-only models remain unexplored in coupled simulations, where tropical cyclone intensity also varies significantly with subsurface ocean conditions. Firstly, boundary-layer dynamics exert control on the location of the updraught at the top of the boundary layer, which determines the location of the eyewall updraught. The location and strength of the eyewall updraught influence the radial advection of absolute angular momentum, M, above the boundary layer, a region where M is approximately conserved. If the eyewall updraught is strong enough, M is advected inwards. Otherwise, M is advected outwards. Secondly, the dynamics of the boundary-layer flow influences the surface latent heat flux, which depends inter alia on the near-surface wind speed. Since the surface latent heat flux also depends on subsurface ocean conditions, these two aspects motivate a closer examination of the boundary layer in coupled atmosphere–ocean models.

Studies using coupled atmosphere–ocean models established early on that the wind-stress-induced sea-surface cooling associated with tropical cyclones leads to a decrease in tropical cyclone intensity (Chang and Anthes, 1979; Khain and Ginis, 1991; Bender et al., 1993). The decrease can be significant, with tropical cyclone intensity up to 50% less compared with the case in which there is no sea-surface cooling (Schade and Emanuel, 1999). Capturing the sea-surface cooling in coupled models has improved tropical cyclone intensity forecasting, which previously relied on atmosphere-only models (Bender and Ginis, 2000; Mogensen et al., 2017; Balaguru et al., 2018), considerably.

The sea-surface cooling initiated by the tropical cyclone depends on pre-storm subsurface ocean conditions. This is because the subsurface ocean structure influences the ocean processes that are primarily responsible for sea-surface cooling. These processes include entrainment, vertical mixing, and upwelling associated with Ekman pumping, where cooler thermocline waters ascend into the mixed layer due to the divergence of warmer surface waters (Price, 1981). Furthermore, the subsurface

ocean structure is shaped by background ocean eddies, which are predominantly found near major current systems. Warm-core eddies can limit the sea-surface cooling, whereas cold-core ocean eddies can enhance the sea-surface cooling (Jaimes and Shay, 2009; Jaimes et al., 2015; 2016; Ma et al., 2017). Consequently, background eddies impact tropical cyclone intensity, as shown in numerical models of varying complexity (Lin et al., 2005; Wu et al., 2007; Yablonsky and Ginis, 2012; Ma et al., 2013; Yan et al., 2017). Warm-core eddies are of particular interest, because they are favourable for rapid intensification, particularly if the background, climatological ocean mixed layer is not deep (Lin et al., 2008). Given its impact on sea-surface cooling and tropical cyclone intensity, the subsurface ocean structure is considered to be of first-order importance for tropical cyclone intensity forecasting (Emanuel, 1999).

Sea-surface cooling influences tropical cyclone intensity by reducing the surface latent heat flux between ocean and atmosphere, which is the primary energy source for tropical cyclones (Emanuel, 1986). However, the process by which tropical cyclone intensity changes is far from straightforward. Recent studies using coupled models turn to Emanuel's influential paradigm to explain changes in tropical cyclone intensity due to a cold wake (Emanuel, 1989; 1995; 1997; Lee and Chen, 2014; Chen et al., 2017; Li and Huang, 2019). However, one shortcoming of this paradigm is that, while considering boundary-layer thermodynamics, it does not recognise the importance of atmospheric boundary-layer dynamics to spin up (Montgomery and Smith, 2014).

Boundary-layer dynamics exert a strong control on the radius at which the boundary-layer inflow turns upwards into the eyewall updraught (Zhang et al., 2001; Nguyen et al., 2002; Smith et al., 2009; Persing et al., 2013; Abarca et al., 2015; Zhang and Marks, 2015; Schmidt and Smith, 2016). The thermodynamic characteristics of the updraught out of the boundary layer determine the rate of diabatic heating within the eyewall updraught (Smith and Montgomery, 2016). The boundary-layer updraught also advects tangential momentum vertically, which contributes significantly to spin-up in the eyewall updraught, provided sufficiently large tangential momentum is generated in the boundary layer (Smith et al., 2009; Persing et al., 2013; Kilroy et al., 2016; Schmidt and Smith, 2016). The tight coupling between the boundary layer and the eyewall updraught is underscored further by the finding that spin-down occurs if the eyewall updraught is not strong enough to accept the boundary-layer updraught (Smith and Wang, 2018).

Another important aspect of boundary-layer dynamics is the lack of gradient wind balance in the boundary layer. As a result, nonlinear advective terms cannot be

---

[1] The grid spacing in ICON is defined as the square root of the area of the triangular cells and is almost constant over the globe.

neglected from the momentum equations in the boundary layer (Vogl and Smith, 2009). Kilroy *et al.* (2016) demonstrated with an atmosphere-only model that nonlinear boundary-layer dynamics lead to nonlocal effects, whereby the expanding outer circulation leads to an increasing radius of forced ascent of boundary-layer air at the base of the eyewall updraught. By controlling the radius of forced ascent, boundary-layer dynamics play an active role in the radially outward movement of the eyewall updraught and, ultimately, the accompanying decrease in tropical cyclone intensity.

Although boundary-layer dynamics has been shown to play an important role for the radially outward movement of the eyewall updraught in atmosphere-only simulations, its role has not been examined in coupled simulations. Recent studies of the tropical cyclone cold wake attribute the radially outward movement of the eyewall updraught to decreasing surface latent heat flux and the accompanying weakening deep convection in the eyewall updraught (Chen *et al.*, 2010; 2017; Li and Huang, 2018; Guo *et al.*, 2020; Ma, 2020). While these studies do examine the role of boundary-layer dynamics in determining the moisture transported inwards by the boundary layer, they do not examine the role of boundary-layer dynamics in determining the inner-core expansion. However, the foregoing discussion indicates that it is crucial to consider both boundary-layer dynamics and air–sea coupling to understand the inner-core expansion and the accompanying change in tropical cyclone intensity.

In this study, we investigate the influence of boundary-layer dynamics and air–sea coupling on the change in the location of the eyewall updraught and the intensity of a mature tropical cyclone. To this end, we use a simulation of a tropical cyclone run with the fully coupled ICOsahedral Nonhydrostatic (ICON) model in a global configuration with 5-km horizontal grid spacing for both atmosphere and ocean (Zängl *et al.*, 2015; Korn, 2017). The initialization of the atmosphere and ocean component of the ICON model includes a detailed subsurface ocean structure ahead of the tropical cyclone. The simulated tropical cyclone generates a cold wake that is sensitive to the initial subsurface ocean structure, which includes a warm-core eddy.

A description of the coupled ICON model and the simulation is provided in Section 2. To set the scene for interpreting the simulation, we outline a simple conceptual framework to understand the coupling between the surface latent heat flux, the deep convection in the eyewall updraught, and the boundary-layer flow in Section 3. This framework extends an existing framework to include the additional effects of atmosphere–ocean coupling. In Section 4, we present results from the ICON simulation for the ocean and the atmosphere, and we discuss the change

in tropical cyclone intensity in the context of the conceptual framework. In Section 5, we extend the study by Kilroy *et al.* (2016) and run a steady-state, axisymmetric slab boundary-layer model with a prescribed tangential wind field (Smith, 2003). Prescribing the tangential wind field from the ICON simulation allows us to investigate the role of nonlinear boundary-layer dynamics in controlling the radii of forced ascent and influencing the change in location of the eyewall updraught. A summary and conclusion follows in Section 6.

2 | ICON MODEL DESCRIPTION AND SIMULATION

To study the evolution of a mature tropical cyclone, we analyse a single tropical cyclone from an existing 40-day simulation that was run as part of the development of the 5-km, global, coupled atmosphere–ocean ICON model (Zängl *et al.*, 2015; Korn, 2017). The global configuration allows us to avoid problems arising from a mismatch of physics between a nested region of interest and its boundaries (Emanuel, 2013). We chose this particular simulation because the tropical cyclone in question encounters a warm-core eddy, which provides a compelling case study of tropical cyclone intensity in a coupled model.

Although coupled simulations of tropical cyclones exist with a smaller horizontal grid spacing of 2–3 km, this is the first study of a tropical cyclone simulated in a global domain with no nesting and a grid spacing as low as 5 km for both the atmosphere and the ocean (Chen *et al.*, 2017; Li and Huang, 2019). Because horizontal diffusion parametrised in boundary-layer schemes typically scales with the horizontal grid spacing in mesoscale models, simulated tropical cyclone intensity can increase when the horizontal grid spacing is decreased (Rotunno *et al.*, 2009). At the same time, the effect on tropical cyclone intensity of decreasing the horizontal grid spacing may be limited, due to factors that favour intensification at smaller grid spacing being compensated by factors that favour weakening (Fierro *et al.*, 2009). Since our goal is to articulate the importance of boundary-layer dynamics for tropical cyclone intensity in a coupled simulation by analysing the qualitative behaviour of the processes outlined in the conceptual framework (Section 3), reducing the grid spacing is unlikely to change our analysis.

In the ICON simulation, there are 70 vertical levels in the atmosphere with a model top located at a height of 30 km. Nine of these vertical levels lie below 1 km, permitting adequate resolution of the boundary-layer flow. The ocean part of the model has 128 vertical levels, of which 12 are in the uppermost 100 m, and takes into account bottom topography with a maximum depth of 6,400 m. The atmosphere and ocean are initialised separately prior to

coupling. The atmosphere is initialised with ERA-Interim reanalysis corresponding to August 1, 2013 (Dee *et al.*, 2011). During spin-up of the ocean (not to be confused with tropical cyclone spin-up), the ocean is forced by climatological atmospheric fields. The initialisation of the ocean recreates background oceanic features, including ocean eddies and currents. After the spin-up of the ocean, the atmosphere and ocean are coupled and the model is run for 40 simulation days. Significant computational resources were required for the coupled simulation. A total of 420 nodes were utilised on the Mistral High Performance Computing system at the German Climate Computing Centre (DKRZ), yielding 30 simulated days per day.

Fluxes between the atmosphere and the ocean component are exchanged every 15 minutes. The ICON physics package is, in terms of simulated physical processes, identical to the package incorporated into the ECHAM atmospheric general circulation model that was developed at the Max Planck Institute for Meteorology (Giorgetta *et al.*, 2018). Vertical transport at subgrid scales via turbulent motion is parametrised as turbulent diffusion. The turbulence closure scheme implemented is outlined in Mauritsen *et al.* (2007) and Pithan *et al.* (2015). The tuning of vertical diffusion is achieved through adjustment of the neutral Prandtl number, which is set to 0.7 in our simulation. While the ocean component of ICON resolves long surface gravity waves, short surface gravity waves, in particular breaking surface waves, are not resolved. However, a parametrisation for the turbulent kinetic energy source caused by these breaking waves is applied as a simple source term in the turbulent kinetic energy equation of the Gaspar mixing scheme.

The cloud microphysics package includes warm-rain processes and the formation of cloud ice, but no graupel or hail. Although the inclusion of graupel does lead to more intense tropical cyclones, the difference in the simulated intensification rate and final intensity between a 2-ice and 3-ice scheme of the same type is small for strong tropical cyclones (Wang, 2002; Tao *et al.*, 2011). The low sensitivity of the intensification rate and final tropical cyclone intensity may be due to the different microphysics schemes resulting in similar vertical profiles of diabatic heating and similar levels of downdraughts (Wang, 2002). Moreover, tropical cyclone intensity is significantly more sensitive to changes in the downdraught due to the evaporation of rain and cloud water or the melting of ice hydrometeors (Zhu and Zhang, 2006). Another limitation of this model version is that rainwater cannot be advected horizontally. However, the lack of horizontal rainwater advection is likely to have a negligible effect on the distribution of diabatic heating, because water vapour can still be advected horizontally. This means that rainwater that evaporates

into water vapour can then be advected horizontally into neighbouring grid cells, before recondensing into rainwater. Given that the distribution of clouds and precipitation in tropical cyclones is determined to a large extent by vertical mass transport (Houze, 2010), the effect of this limitation on the azimuthally averaged distribution of water in a mature tropical cyclone is likely to be minimal.

After performing the analysis of the current simulation, an error was found in the model code relating to the calculation of the wind stress. While the wind stress passed to the atmosphere used the ocean velocity with the wrong sign and an incorrect prefactor, the wind stress passed to the ocean did not include the ocean velocity at all. However, since the atmospheric velocity of the tropical cyclone at the surface is much larger than the underlying ocean velocity, the error in the wind-stress magnitude is relatively small. We do not expect that this error matters for our diagnostics.

3 | A CONCEPTUAL FRAMEWORK FOR UNDERSTANDING TROPICAL CYCLONE INTENSITY CHANGE

To interpret the evolution of a tropical-cyclone-like vortex in any complex numerical simulation of the type examined here requires a suitable conceptual framework. The framework adopted here is the so-called rotating-convection paradigm (Montgomery and Smith, 2017), which is an extension of the cooperative paradigm of Ooyama (1969; 1982). The extension applies to a three-dimensional flow configuration and includes a boundary-layer spin-up mechanism as articulated by Smith *et al.* (2009). Within this framework, we recognise explicitly the role of nonlinear boundary-layer dynamics in controlling the change in the radius of forced ascent at the top of the boundary layer on account of the expanding outer circulation (Kilroy *et al.*, 2016). We extend the framework to consider the effect of atmosphere–ocean coupling on tropical cyclone intensity. This framework has not been used previously to investigate the change in simulated tropical cyclone intensity for coupled atmosphere–ocean models and can be understood as follows.

1. *Air–sea coupling*. Surface latent heat supplied to the tropical cyclone depends on the sea-surface temperature (SST), the near-surface wind speed, and the near-surface moisture content. Changes in the surface latent heat flux lead to changes in the equivalent potential temperature, θ_e, in the boundary layer. The value of θ_e determines the buoyancy acquired by the air parcels in the boundary layer and whether they reach the level of free convection. Air parcels that do not reach the level of free convection

remain negatively buoyant. Those that reach the level of free convection become positively buoyant and rise into the troposphere with a vertical velocity that depends on θ_e.

2. *Boundary-layer convergence via surface drag.* Surface drag leads to an inflow in the boundary layer. Due to the upward pressure-perturbation force that follows from mass continuity, the converging air is accelerated out of the boundary layer. The resulting vertical mass flux at the top of the boundary layer, $\overline{\rho w}_{\mathrm{BL}}$, depends, in part, on the strength of convergence in the boundary layer. The strength of convergence and the radial location at which the air is directed upwards are determined to a large extent by the nonlinear dynamics of the boundary-layer flow and the expanding outer circulation.

3. *Boundary-layer convergence via eyewall suction.* In addition to the convergence pushing out air mass from the boundary layer, deep convection in the eyewall updraught acts to suck air mass at the top of the boundary layer into the eyewall updraught above (Smith and Montgomery, 2015). Consequently, $\overline{\rho w}_{\mathrm{BL}}$ depends on boundary-layer convergence via both surface drag and eyewall suction, effects that cannot be separated because of the nonlinearity of the flow dynamics.

4. *Vertical mass flux.* In contrast to $\overline{\rho w}_{\mathrm{BL}}$, the vertical mass flux in the eyewall updraught, $\overline{\rho w}_{\mathrm{EW}}$, is primarily buoyancy-driven and, therefore, more sensitive to changes in θ_e and ultimately air–sea coupling than to changes in $\overline{\rho w}_{\mathrm{BL}}$. The change in $\overline{\rho w}_{\mathrm{EW}}$ also depends on how the areal extent of the eyewall updraught changes. The vertical mass fluxes are important because they influence the evolution of the tropical cyclone structure. Due to mass continuity, mass flows out above the boundary layer if $\overline{\rho w}_{\mathrm{EW}}$ is smaller than $\overline{\rho w}_{\mathrm{BL}}$. Conversely, if $\overline{\rho w}_{\mathrm{EW}}$ is greater than $\overline{\rho w}_{\mathrm{BL}}$, there is inflow above the boundary layer.

5. *Advection of absolute angular momentum.* Any change of the inflow or outflow above the boundary layer is reflected in the radial advection of absolute angular momentum, M. A weakening inflow above the boundary layer decreases the ability of the tropical cyclone to advect M-surfaces radially inwards. Conversely, a strengthening inflow enhances the ability of the tropical cyclone to advect M-surfaces radially inwards.

6. *Tangential velocity change.* The radial advection of M-surfaces translates into local changes in the tangential velocity, v, which can be seen in the following expression for v in terms of M in the f-plane approximation,

$$v = \frac{M}{r} - \frac{1}{2}fr. \tag{1}$$

The radius and Coriolis parameter are given by r and f, respectively.

7. *Feedback on air–sea coupling.* Finally, the local change in the tangential velocity above the boundary layer leads to a change in the radial pressure gradient at the top of the boundary layer (assuming the flow is in approximate gradient-wind balance). This radial pressure gradient is transmitted into the boundary layer and leads to a change in the net radial force there. Through nonlinear boundary-layer dynamics, the change in the net radial force and the expanding outer circulation determine the change in the boundary-layer convergence and the radius of forced ascent. Since the accompanying change in the near-surface wind field influences the radial distribution of surface latent heat flux and, therefore, the air–sea coupling outlined in Equation 1, the interaction between the boundary-layer flow and surface latent heat flux forms a feedback loop.

Within this framework, the intensification of a mature tropical cyclone over a warm-core eddy can be understood as follows (please refer to Figure 1). A higher surface latent heat flux leads to an increase in θ_e at the top of the boundary layer via air–sea coupling. Air parcels with higher θ_e then ascend from the boundary layer into the eyewall updraught at the radius of forced ascent. The vertical mass flux at the top of the boundary layer depends on the convergence due to surface friction and the suction effect of deep convection in the eyewall updraught. Assuming there is no warming aloft, the increase in mean θ_e of air parcels ascending into the eyewall leads to an increase in mean vertical velocity in the eyewall updraught and, if the areal extent of the eyewall updraught does not decrease appreciably, an increase in the vertical mass flux. The inflow and the inward advection of M increase in a vertical layer above the boundary layer at radii outside the eyewall updraught. The corresponding increase in the local tangential velocity increases the radial pressure gradient transmitted into the boundary layer, which changes the net radial force there. The change in the net radial force, along with the expanding outer circulation, leads to a change in the boundary-layer convergence and the radius of forced ascent. While one may expect an increase in the transmitted radial pressure gradient to increase the strength of the boundary-layer convergence and decrease the radius of forced ascent, one cannot know whether this is the case until one performs the calculation, due to the nonlinear nature of boundary-layer dynamics. A strengthening in the boundary-layer convergence would feedback on air–sea coupling, with increasing near-surface wind speed increasing the surface latent heat flux, assuming a constant moisture disequilibrium at the air–sea interface. In reality, moisture disequilibrium is not constant and increases in moisture disequilibrium can be a more efficient way of increasing surface latent heat flux than near-surface wind speed (Jaimes *et al.*, 2021).

As shown in Figure 1, the decay of a mature tropical cyclone due to a cold wake or interaction with a cold-core
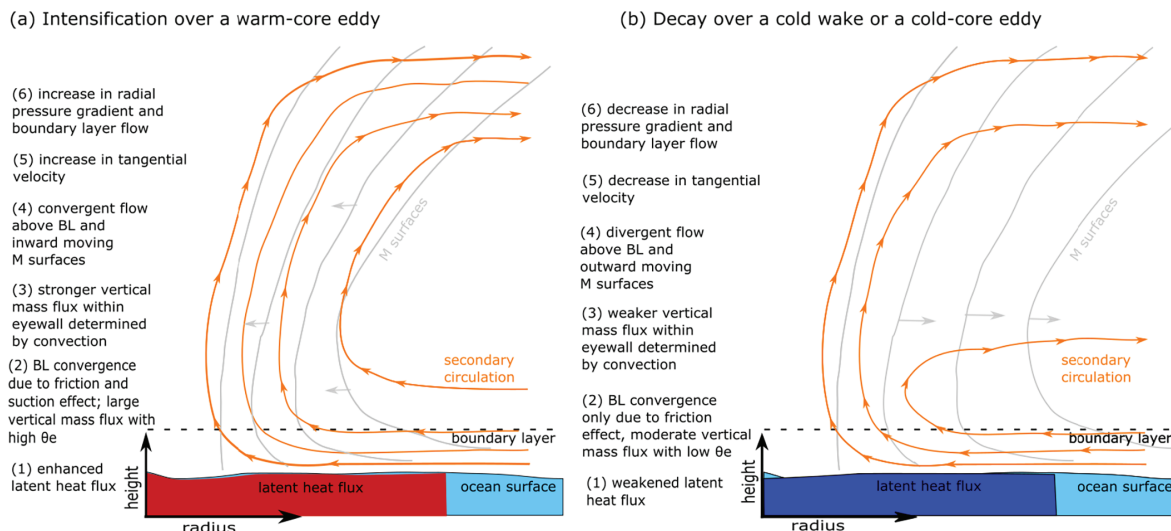
FIGURE 1 Schematic of the processes outlined in the conceptual framework in the case of (a) intensification over a warm-core eddy and (b) decay over a cold wake

eddy can be understood with the same set of processes, but with the tendencies reversed. Again, although one might expect a weakening of boundary-layer convergence and an increase in the radius of forced ascent, one cannot be sure, due to the nonlinear nature of boundary-layer dynamics. In the case of weakening boundary-layer convergence, a negative feedback may occur between the surface latent heat flux and the near-surface wind speed. Note, however, that a negative feedback might also arise for fixed SST, if convergence in the boundary layer is initially strong and $\overline{\rho w}_{BL}$ is greater than $\overline{\rho w}_{EW}$. In this case, there is an outflow above the boundary layer that spins down the boundary-layer flow (Kilroy *et al.*, 2016; Smith and Wang, 2018).

4 | TROPICAL CYCLONE IN THE ICON SIMULATION

The tropical cyclone simulated in the coupled ICON model is shown in Figure 2. It forms in the North Atlantic in the last 10 days of the 40-day simulation, between August 31 and September 9, 2013. These dates coincide with the historical North Atlantic tropical storm *Gabrielle*. In our simulation, the tropical cyclone intensity is considerably larger than in *Gabrielle* and follows a trajectory that runs much closer to the eastern seaboard of North America, as seen in Figure 2. However, the synoptic forecasting skill of the model is marginal by day 30, and the synoptic ocean eddy field does not represent the ocean eddy field from 2013. Therefore, the simulated tropical cyclone cannot be expected to correspond to any historical tropical cyclone, including tropical storm *Gabrielle*.
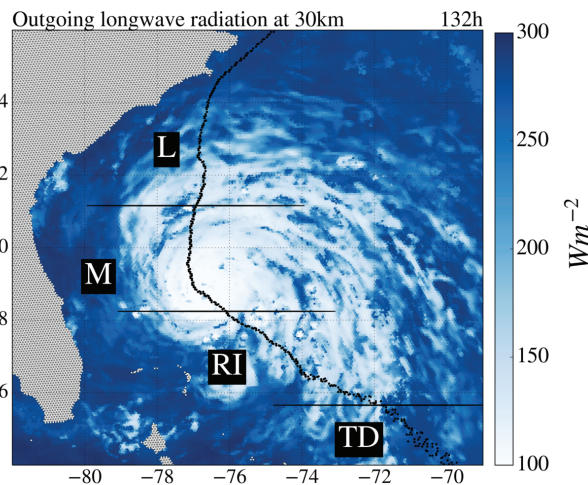

FIGURE 2 The outgoing longwave radiation at a height of 30 km, corresponding to the model top, is shown for 132 hr after August 31, 2013, 0000 UTC. The tropical cyclone traverses along the trajectory (dotted line) to higher latitudes. The partitions between stages (see Table 1) are indicated with solid horizontal lines. Here, the data are plotted on the original triangular grid, and land cells are masked out in gray

In this section, we start with a brief overview of the tropical cyclone in the ICON simulation, including its intensity, structure, and environment (Section 4.1). Then we investigate the change in tropical cyclone intensity with the help of the conceptual framework outlined in Section 3, focusing on the period where the tropical cyclone generates a cold wake and encounters a warm-core eddy. Our investigation consists of three steps. Firstly, we examine the role of the ocean in the surface latent flux supplied to the tropical cyclone. Here, we analyse the pre-storm upper-ocean structure (Section 4.2) and
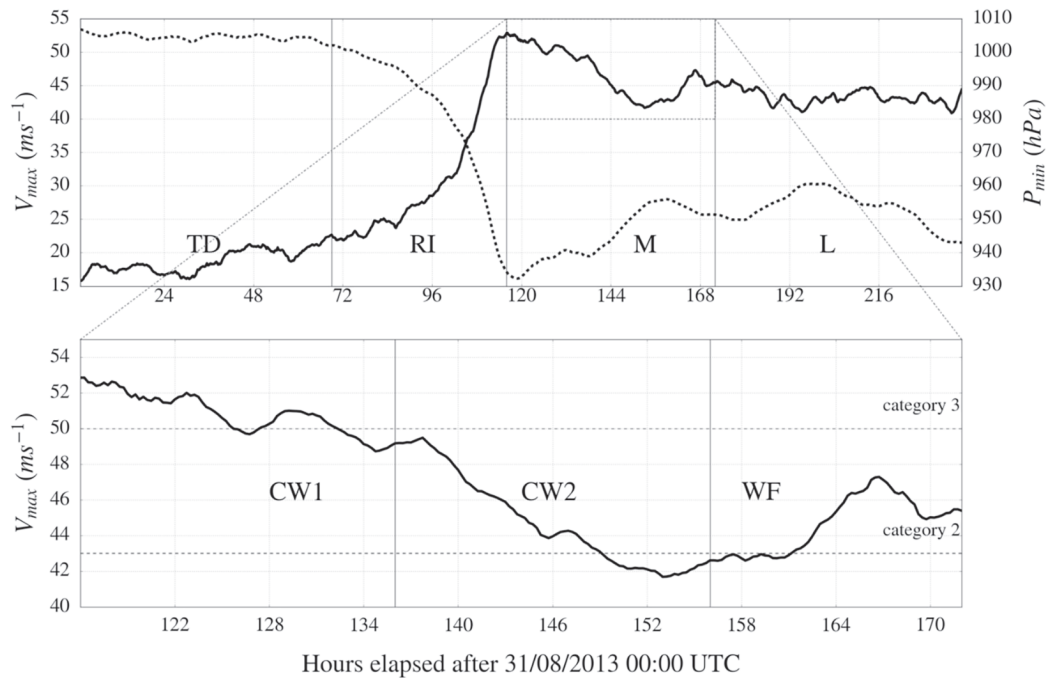
FIGURE 3 Top: the 3-hr running mean of the maximum near-surface wind speed, V_{max}, and the minimum sea-level pressure, P_{min}, are denoted by a solid line and a dashed line, respectively. Bottom: a blow-up of the maximum near-surface wind speed in the mature phase (M). A description of the abbreviations is provided in Table 1

discuss the coupling between the sea-surface cooling and the surface latent heat flux (Section 4.3). Secondly, we focus on the atmospheric processes that are listed in the conceptual framework, including the thermodynamics of the ascending boundary-layer air (Section 4.4), the vertical mass fluxes in the eyewall updraught (Section 4.5), the secondary circulation in and above the boundary layer (Section 4.6), and the advection of absolute angular momentum (M) at the top of the boundary layer (Section 4.7). Finally, we draw on our analysis of both the ocean and the atmosphere to discuss the combined importance of ocean–atmosphere coupling and boundary-layer dynamics for the change in tropical cyclone intensity (Section 4.8).

4.1 | Overview of the simulated tropical cyclone

A time series of tropical cyclone intensity is shown in Figure 3. Two conventional measures of tropical cyclone intensity are displayed: the minimum mean sea-level pressure at the centre, P_{min}, and the maximum 10-m wind speed, V_{max}. Between 92 and 116 hr the tropical cyclone undergoes rapid intensification, defined as an increase in V_{max} of more than 15.4 m·s^{-1} within 24 hr, into a category 3 hurricane with a peak V_{max} of 52 m·s^{-1} and a P_{min} of 933 hPa (Kaplan and DeMaria, 2003). In the mature

phase, V_{max} initially decreases between 116 and 152 hr: gradually until 136 hr, and then more dramatically up to 152 hr. During this period, the tropical cyclone weakens into a category 2 hurricane. In the final part of the mature phase, the tropical cyclone reintensifies by around 6 m·s^{-1} between 152 and 166 hr.

We subdivide the tropical cyclone intensity time series into several phases listed in Table 1. We define the tropical depression phase to be the initial phase before the radius of gales is well defined. The radius of gales refers to the radius at which the wind speed crosses a threshold of 17 m·s^{-1}. The tropical depression phase (TD) is followed by the rapid intensification phase (RI), where the radius of gales is well defined. Since the radius of gales is computed from an azimuthal mean, unlike V_{max}, the start of the rapid intensification phase does not coincide exactly with V_{max} exceeding 17 m·s^{-1}. We define the subsequent mature phase to start when V_{max} reaches its peak value at 116 hr and to end at 172 hr, when the tropical cyclone makes landfall. The mature phase is further subdivided into three subphases. During the cold wake 1 (CW1) phase, the tropical cyclone gradually decays. The tropical cyclone experiences a more rapid decay in the cold wake 2 (CW2) phase. Finally, in the warm feature (WF) phase, the tropical cyclone reintensifies.

Figure 4 displays horizontal snapshots of vertical velocity and tangential velocity taken at a height of 5 km. The first two panels show the development of a symmetric

TABLE 1 A list of phases that the simulated tropical cyclone undergoes during its life cycle

Stage	Time (hours after August 31, 2013, 0000 UTC)	Intensity trend	Maximum near-surface wind speed (m·s^{-1})
Tropical Depression (TD)	0–69	Nascent tropical cyclone strengthens into tropical storm	15–22
Rapid Intensification (RI)	69–116	Sustained intensification, including instance of rapid intensification	22–52
Mature (M): Cold Wake 1 (CW1)	116–136	Gradual decay	49–52
Mature (M): Cold Wake 2 (CW2)	136–156	Accelerated decay	42–50
Mature (M): Warm Feature (WF)	156–172	Reintensification	42–48
Landfall and Recurvature (L)	172–240	Steady	42–45
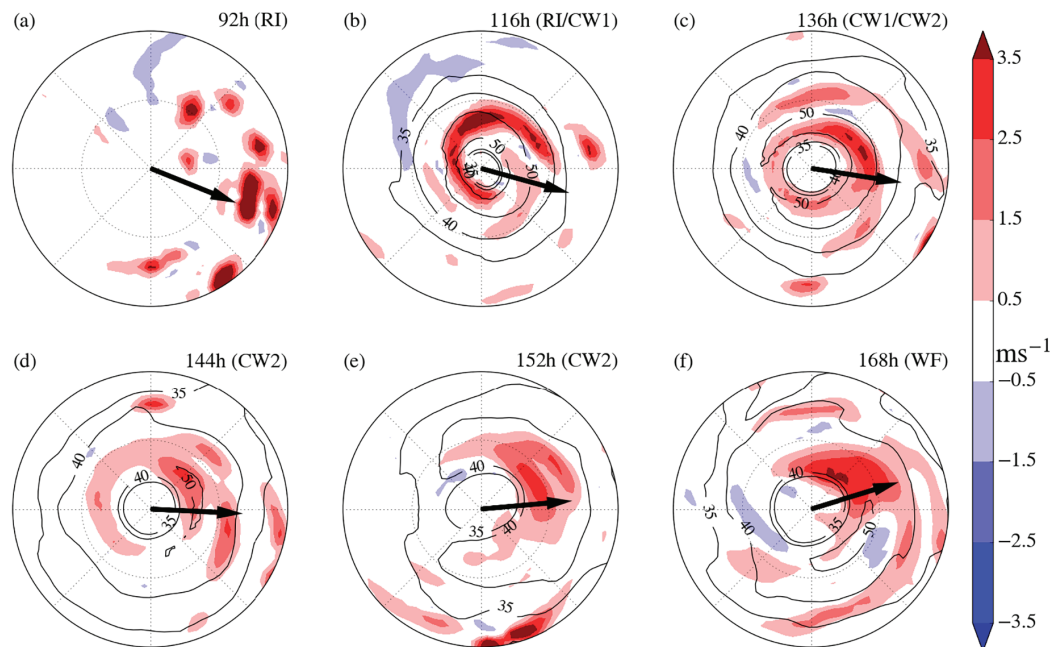
FIGURE 4 Horizontal snapshots of vertical velocity (blue and red shading) and tangential velocity (black contours) at a height of 5 km at (a) 92, (b) 116, (c) 136, (d) 144, (e) 152, and (f) 168 hr after August 31, 2013, 0000 UTC. For the tangential velocity, contours are shown for 35 m·s^{-1}, 40 m·s^{-1}, and 50 m·s^{-1}. The direction of the vertical wind shear, as defined by Kaplan and DeMaria (2003), is indicated by the arrow. Radial grid lines are displayed for 50 and 100 km

eyewall updraught during RI (Figure 4a,b). The transition from an asymmetric structure to a symmetric eyewall updraught is characteristic of the transition into a mature tropical cyclone (Houze, 2010). The decreasing vertical velocity in the eyewall updraught region during CW1 and CW2 indicates weakening deep convection (Figure 4b–d). Regions of strong convection remain, but these are found away from the eyewall updraught at radii beyond 100 km, where the 30 m·s^{-1} tangential velocity contour is located. Towards the end of CW2, convection in the eyewall updraught begins to strengthen, with a substantial increase in vertical velocity visible during the WF (Figure 4 e,f).

The azimuthal-mean structure of the absolute angular momentum (M) surfaces and the secondary circulation is shown in Figure 5. As is typical of tropical cyclones, the M-surfaces slope outwards with height and generally have a positive radial gradient. A region of strong inflow is found at the sea surface and a region of outflow is located in the upper troposphere. Connecting the inflow and outflow regions is a region of updraught at small radii that extends vertically throughout the depth of the troposphere. As the secondary circulation strengthens and the eyewall updraught develops during RI, the M-surfaces move radially inwards, indicating a strengthening of the primary circulation (Figure 5a,b). During
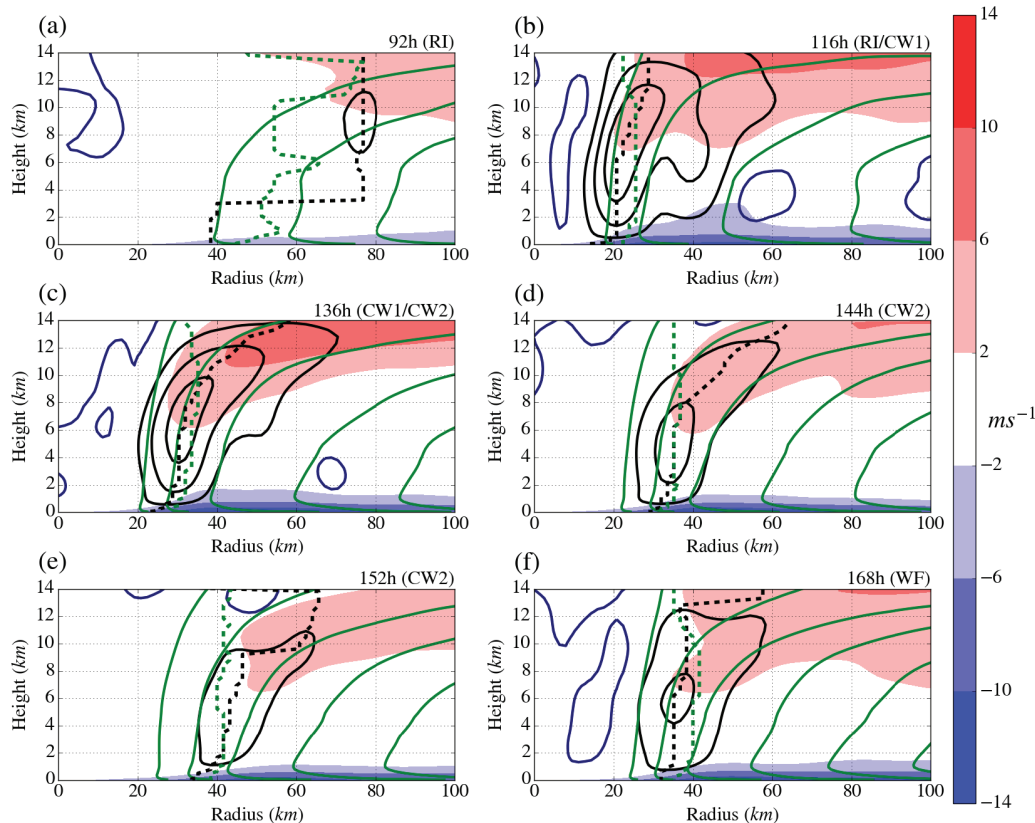
FIGURE 5 Azimuthal mean of flow in a tropical cyclone is shown as a 3-hr running mean for 92, 116, 136, 144, 152, and 168 hr after August 31, 2018, 0000 UTC. Contours of the updraught are shown by solid black lines and correspond to (0.5, 1.0, 1.5) m·s^{-1}. The single blue contour shows regions of downdraught. Angular momentum contours are displayed as solid green lines and increase from the centre outwards, corresponding to (1.0, 1.5, 2.0, 2.5, 3.0) × 10^6 m^2·s^{-1}. The blue and red shading indicates inflow and outflow, respectively. The shading corresponds, from light to dark, to (2, 6, 10, 14) m·s^{-1}. The radius of maximum vertical velocity is indicated by the black dashed line and the radius of maximum tangential velocity is shown as a green dashed line

the subsequent weakening of the eyewall updraught during CW1 and CW2, the eyewall updraught moves radially outwards (Figure 5b–e). Simultaneously, the primary circulation strengthens at larger radii, but weakens at smaller radii, where the M-surfaces move outwards. As the eyewall updraught strengthens during WF, it moves radially inwards (Figure 5e,f). The primary circulation strengthens throughout the tropical cyclone, which is evident from the inward shift of the M-surfaces.

Figure 6 shows the height of the boundary layer, h, diagnosed for the ICON simulation. Here, h is defined as the height at which the maximum tangential velocity in the tropical cyclone is located (Bryan and Rotunno, 2009). During RI, h initially decreases from 1,200 to 600 m. During the remainder of RI and the subsequent mature phase, h fluctuates in a range between 600 and 800 m. The vertical level in the ICON model that corresponds most closely to the upper boundary of h in Figure 6 is located at a height of 780 m. While the boundary-layer height is in reality a function of radius (Zhang *et al.*, 2011), we
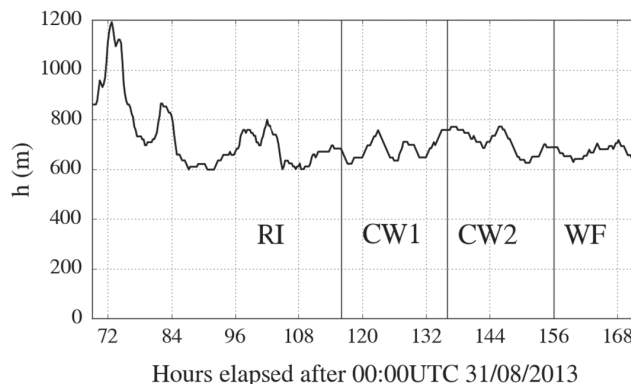

FIGURE 6 Time series of the boundary-layer height, h, displayed as a 3-hr running mean

take h to be a constant 780 m with a view to keeping the subsequent analysis simple.

Figure 7a shows the time series of the surface latent heat flux averaged over an annulus centred on the tropical cyclone centre, which is located at the surface grid
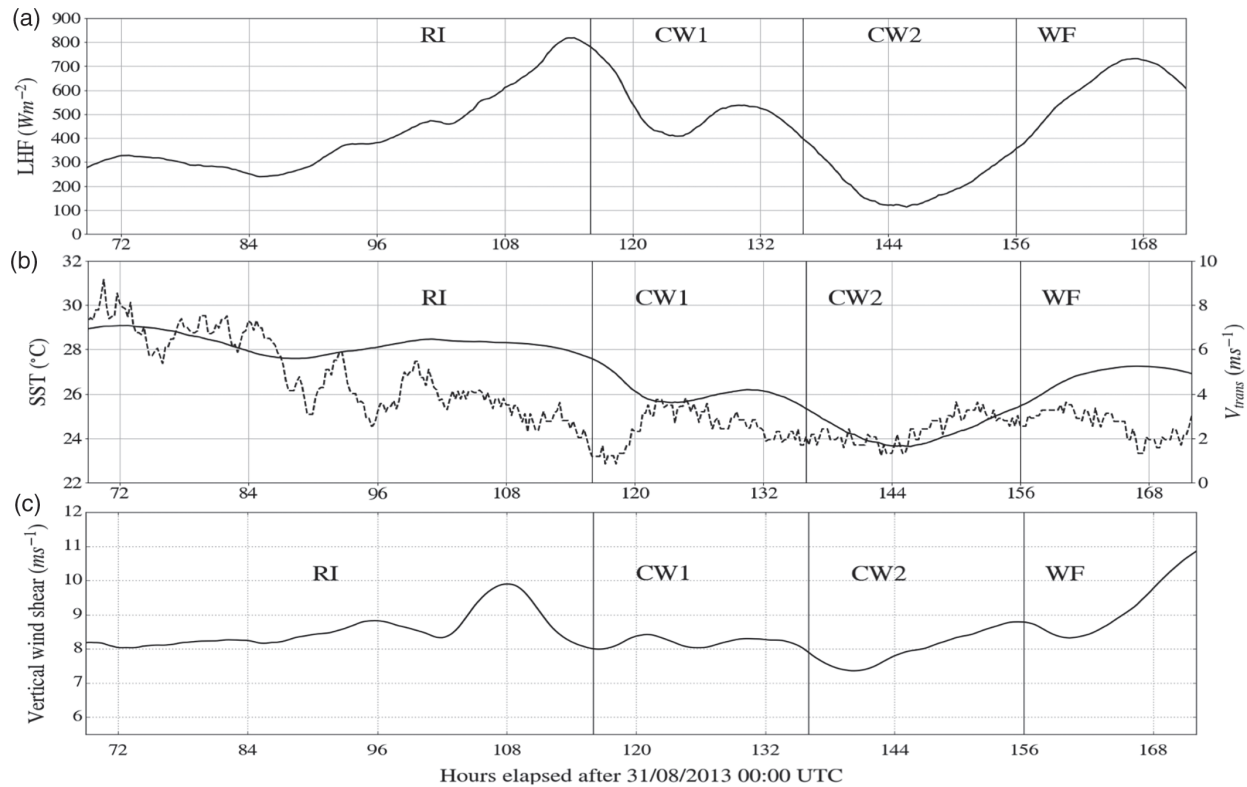
FIGURE 7 Time series of (a) surface latent heat flux (LHF), (b) SST (solid line) and translational speed (V_{trans}), and (c) vertical wind shear. All variables are displayed as 3-hr running means. LHF and SST are averaged over an annulus that extends 10 km inside and 10 km outside the radius of maximum near-surface wind speed. The vertical wind shear is computed from the average horizontal wind vector over a circular anulus spanning a radial interval between 200 and 800 km

cell with the lowest mean sea-level pressure. The annulus has an inner and outer radius that are respectively 10 km less than and 10 km greater than the radius of maximum near-surface wind speed. The surface latent heat flux rises and peaks toward the end of RI at 820 W·m^{-2}. During CW1, the surface latent heat flux reaches a local minimum of around 410 W·m^{-2} and then peaks again at 540 W·m^{-2}. Subsequently, the surface latent heat flux decreases continuously into CW2 and reaches a global minimum of 110 W·m^{-2}. This global minimum is followed by an increase during the latter stage of CW2 and WF, where the surface latent heat flux peaks at 730 W·m^{-2}.

A time series of SST is plotted in Figure 7b. Here, SST is averaged over the same time-varying annulus as for the surface latent heat flux. During RI, SST fluctuates between 29.0 and 27.3 °C. In the mature phase, SST experiences two minima and maxima that coincide with the respective minima and maxima of the surface latent heat flux. During CW1, a local minimum of 25.6 °C is followed by a local maximum of 26.2 °C. Subsequently, SST reaches a global minimum of 23.6 °C during CW2, before recovering and peaking at 27.2 °C in WF

The time series of the translational speed, V_{trans}, is also shown in Figure 7b. A positive correlation and time lag

are evident between SST and V_{trans}. Initially, V_{trans} shows a clear downward trend, decreasing from 9 m·s^{-1} during RI. During the mature phase, a positive correlation and time lag between SST and V_{trans} are evident from a similar set of minima and maxima in V_{trans}. The first minimum at 1 m·s^{-1} occurs at the start of CW1 and is quickly followed by a maximum close to 4 m·s^{-1}. After this maximum, V_{trans} decreases steadily until 144 hr (CW2) to approximately 2 m·s^{-1}. Subsequently, V_{trans} increases in the latter part of CW2 and then remains between 3 and 4 m·s^{-1} until 160 hr (WF).

Figure 7c shows the vertical wind shear of the environment, which is defined as the difference between the average horizontal wind vectors on the 200- and 850-hPa surfaces computed for a radius between 200 and 800 km (Kaplan and DeMaria, 2003). The vertical wind shear remains fairly constant at around 8 m·s^{-1} during CW1, CW2, and the initial stage of WF before increasing.

While the moderate to large vertical wind shear may reduce the maximum tropical cyclone intensity reached in RI (Wong and Chan, 2004), a constant vertical wind shear is unlikely to be responsible for the different decay rates in CW1 and CW2. Since increasing vertical wind shear is associated with decay, the reintensification during WF
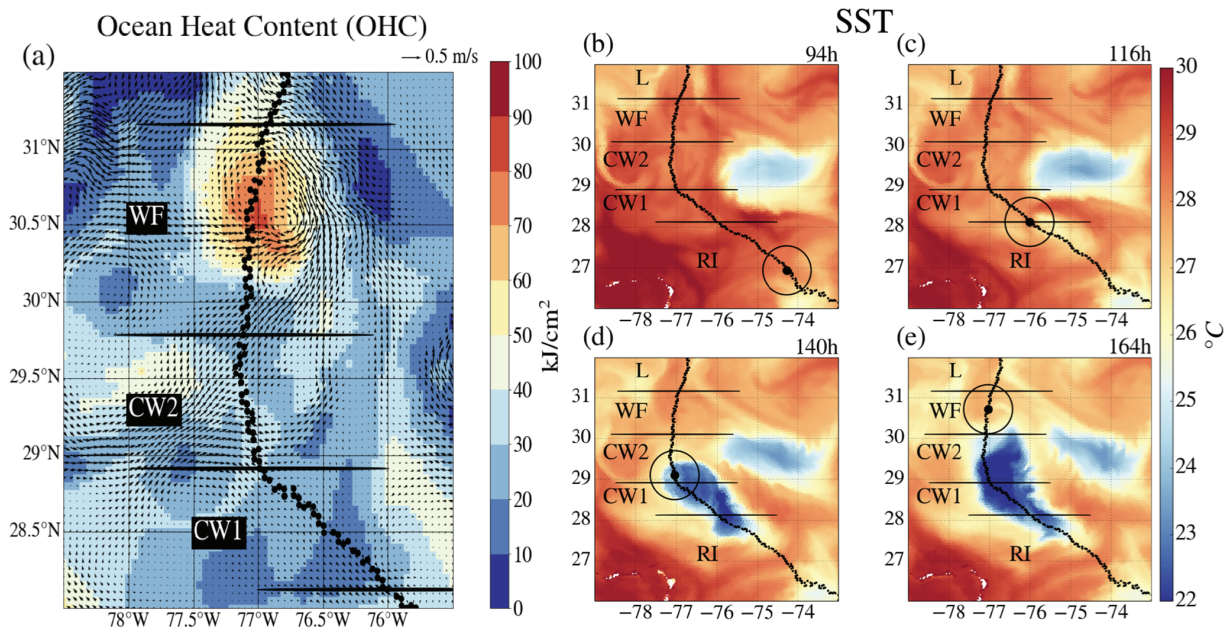
FIGURE 8 Snapshots of (a) pre-storm ocean heat content (OHC) at 0 hr and SST at (b) 94 hr (RI), (c) 116 hr (RI/CW1), (d) 140 hr (CW2), and (e) 164 hr (WF) after August 31, 2013, 0000 UTC. The horizontal surface current is shown in (a) by black arrows. The tropical cyclone traverses northwards along the trajectory indicated by the dotted line in all snapshots. The position of the tropical cyclone is shown by the black circle. The partitions between the stages (see Table 1) are indicated with solid horizontal lines. The SST snapshots are plotted on the original triangular grid

cannot be due to the concurrent increase in vertical wind shear.

Instead, the change in tropical cyclone intensity in the mature phase is strongly correlated to the changes in SST and surface latent heat flux. The decay during CW1 and CW2 occurs as the SST and surface latent heat flux drop, with a faster rate of decay during CW2 coinciding with lower SST and surface latent heat flux than in CW1. Similarly, the reintensification during the latter stage of CW2 and WF is accompanied by increasing SST and surface latent heat flux. There is also a time lag between the change in SST and surface latent flux and the intensity. The peak in intensity at the start of CW1 occurs 2 hr after the surface latent heat flux peaks. During CW2, the intensity only reaches its minimum value 8 hr after both SST and surface latent heat flux do so.

4.2 | Upper-ocean structure and sea-surface cooling

Figure 8a shows the pre-storm upper-ocean heat content, OHC, for the region traversed by the tropical cyclone in the mature phase (CW1, CW2, WF). Values of OHC are computed following Leipper and Volgenau (1972), where OHC is defined as the deviation of the upper-ocean temperature from 26 °C integrated over all depths between the surface and the 26 °C isotherm. Physically, OHC can be interpreted

as the anomalous heat content in the upper ocean where the temperature exceeds 26 °C. The pre-storm OHC does not exceed 40 kJ·cm^{-2} along the section of the trajectory traversed during CW1 and CW2. However, the pre-storm OHC is much larger for the WF section of the trajectory and reaches a maximum between 80 and 90 kJ·cm^{-2}.

The higher pre-storm OHC for the WF section of the trajectory corresponds to a warm-core eddy. Situated at 30.5 °N–77 °E, the warm-core eddy lies directly on the trajectory of the tropical cyclone. The surface current reveals an anticyclonic signature that is characteristic of warm-core eddies (Figure 8a). Although the warm-core eddy is clearly visible from the pre-storm OHC and the sea-surface height (not shown), it is concealed in the pre-storm SST field shown in Figure 8b.

The presence of this concealed, subsurface warm-core eddy reduces the sea-surface cooling locally (Figure 8b–e). The reduced sea-surface cooling is consistent with weaker entrainment cooling in a deeper mixed layer (not shown), where less wind-driven kinetic energy is available for turbulent mixing because more energy is lost to the thermocline via internal near-inertial waves (Linden, 1975; Gill, 1984; Jaimes and Shay, 2009). The higher SST associated with the reduced sea-surface cooling over the warm-core eddy contrasts with the lower SST trailing behind the tropical cyclone (Figure 8e). The lower SST is typical of a cold wake associated with tropical cyclones. In agreement with previous work, the sea-surface cooling is stronger
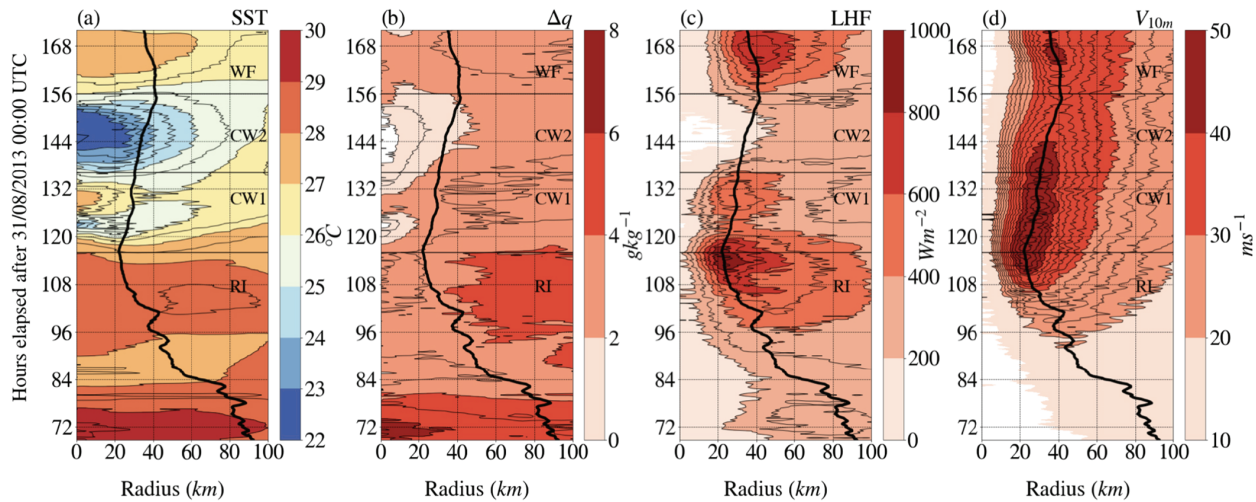
FIGURE 9 Hovmöller plots of azimuthally averaged (a) SST, (b) moisture disequilibrium at the air–sea interface, (c) surface latent heat flux, and (d) near-surface wind speed for the innermost 100 km. The spacings of the thin black contours for each of the plots are (a) 1 °C, (b) 1 g·kg^{-1}, (c), 100 W·m^{-2}, and (d) 2 m·s^{-1}. The 3-hr running mean of the radius of maximum near-surface wind speed, $R_{surf\,max}$, is shown as a thick solid black line in all four plots

on the right-hand side of the trajectory, and the strongest sea-surface cooling is found in the rear part of the cold wake away from the inner core, which is typical for tropical cyclones in the North Atlantic (Chang and Anthes, 1978; Price, 1981; Cione and Uhlhorn, 2003). While the effect of warm-core eddies on the surface latent heat flux and change in intensity has been studied before, this is the first study to examine the influence of a warm-core eddy at depth on the kinematic structure of the boundary layer with a fully three-dimensional eddy-resolving simulation.

4.3 | Influence of sea-surface cooling on surface latent heat flux

Figure 9 shows the azimuthal-mean SST, moisture disequilibrium at the air–sea interface, surface latent heat flux, and near-surface wind speed. During RI, the SST reflects the ambient SST and changes over time, while remaining relatively uniform in the radial direction (Figure 9a). A cold wake signal is evident during CW1 from the lower SST and the positive radial gradient in SST at 120 hr. This cold-wake signal is superseded by an increase in SST and then a second, more prolonged cold-wake signal. The second cold-wake signal displays stronger sea-surface cooling during CW2 than in CW1; note the lower SST and the larger positive radial gradient in SST. The variation in sea-surface cooling may be due to the change in translational speed (Chang and Anthes, 1978; 1979; Price, 1981). The time series in Figure 7b shows that the sea-surface cooling during both CW1 and CW2 follows a decrease in V_{trans}. The stronger sea-surface cooling in CW2 may also

be related to the increasing size of the tropical cyclone (not shown), with the radius of gales increasing from 120 km at the start of CW1 to 250 km at the beginning of CW2 (Pun et al., 2018). During WF, the high SST associated with the subsurface warm-core eddy contrasts with the low SST in CW1 and CW2 (Figure 9a).

The decrease in the moisture disequilibrium at the air–sea interface, Δq, during CW1 and CW2 is positively correlated to the decreasing SST (Figure 9a,b). This correlation is evident from the positive radial gradient seen during CW2 for both SST and Δq inside a 50-km radius. Similarly, the increasing Δq is closely correlated to the increasing SST during the latter stage of CW2 and WF. The change in Δq is reflected by the decrease and increase in the surface latent heat flux during the mature phase (Figure 9b,c). The pronounced change in surface latent heat flux during the mature phase is consistent with the high sensitivity of surface latent heat flux to SST in regions with large near-surface wind speed (Cione and Uhlhorn, 2003).

The correlation between changes in the surface latent heat flux and the near-surface wind speed, V_{10m}, is weaker during the mature phase (CW1, CW2, WF) than in RI (Figure 9c,d). During RI, the increase in the surface latent flux at the radius of maximum near-surface wind speed, $R_{surf\,max}$, is consistent with the simultaneous increase in V_{10m}. At the end of RI, the peak in surface latent heat flux at $R_{surf\,max}$ coincides temporally and spatially with the peak in V_{10m}. At larger radii, the change in the surface latent flux during RI is influenced by changes in Δq. Between 96 and 120 hr, the surface latent heat flux exceeds 400 W·m^{-2} over a region extending from $R_{surf\,max}$ out to 100 km. The
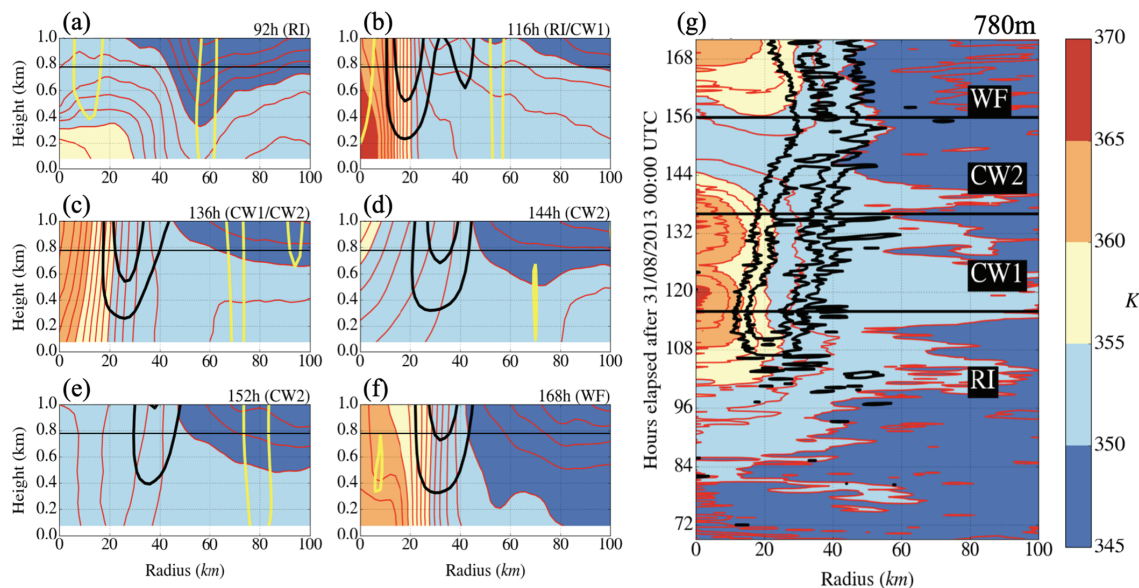
FIGURE 10   The azimuthal-mean of equivalent potential temperature, $\overline{\theta}_e$, and vertical velocity are displayed as (a–f) six instantaneous radius–height snapshots and (g) a Hovmöller plot at the boundary-layer top at 780 m. The vertical snapshots are shown for (a) 92, (b) 116, (c) 136, (d) 144, (e) 152, and (f) 168 hr after August 31, 2013, 0000 UTC. The horizontal black lines indicate the top of the boundary layer at 780 m. Note that the color bar and contour values are identical for both the vertical snapshots and the Hovmöller plot. The spacing between the red $\overline{\theta}_e$ contours is 1 K in panels (a)–(f) and 2.5 K in panel (g). The thick black contours in (a)–(g) correspond to an updraught of 0.25 and 0.5 m·s^{-1}. The bright yellow contour in panels (a)–(f) indicates regions of downdraught (zero vertical velocity). For visual clarity, the yellow contour is not included in panel (g)

radial extent of the 400 W·m^{-2} contour decreases substantially in the latter part of CW1. This decrease is consistent with the simultaneous decrease in SST and Δq, rather than the local increase in V_{10m} seen from the expanding contours in Figure 9d. While the maximum surface latent heat flux occurs at $R_{surf\,max}$ during CW1, the same is not true for CW2. Instead, the maximum surface latent heat flux during CW2 occurs at a radius larger than $R_{surf\,max}$, because the surface latent heat flux is dominated by the decrease in SST and Δq. During the latter stage of CW2 and WF, the sudden increase in surface latent heat flux from $R_{surf\,max}$ out to 100 km cannot be explained by a sudden local increase in V_{10m}, but rather by the jump in SST and Δq. More generally, this period of reintensification is an example of increasing SST and Δq being an effective way to increase the surface latent heat flux in a warm-ocean regime (Jaimes *et al.*, 2021). The foregoing analysis shows that the change in the areal-averaged surface latent heat flux in Figure 7a is dominated by changes in SST and Δq in the mature phase.

4.4 | Equivalent potential temperature of ascending boundary-layer air

The changes in the surface latent heat flux lead to changes in the equivalent potential temperature, θ_e, in

the boundary layer, which in turn determine the buoyancy of air parcels there. Only air parcels with positive buoyancy at the top of the boundary layer are able to rise into the eyewall updraught, with a vertical velocity that depends on the magnitude of the buoyancy. Figure 10 shows radius–height snapshots and a Hovmöller plot at the boundary-layer top for the azimuthal-mean equivalent potential temperature, $\overline{\theta}_e$, and the vertical velocity. As the tropical cyclone intensifies and becomes increasingly axisymmetric during RI, the radial gradient of $\overline{\theta}_e$ becomes negative throughout the innermost 100 km (Figure 10a,b,g). The largest negative radial gradient is found inside a 20-km radius, where the $\overline{\theta}_e$ contours become increasingly vertical throughout the depth of the boundary layer. During CW1, the decreasing average surface latent heat flux is accompanied by a decrease in $\overline{\theta}_e$ inside a 20-km radius: note how the dark red shading in the inner core disappears and the negative radial gradient decreases (Figure 10b,c,g). In contrast, $\overline{\theta}_e$ continues to increase between a 20 and 40-km radius throughout the depth of the boundary layer. At radii beyond 40 km, the $\overline{\theta}_e$ contours are not vertical and the boundary layer is not well mixed. During CW2, the decrease in the average surface latent heat flux to a global minimum is accompanied by a substantial drop in $\overline{\theta}_e$ inside a 40-km radius throughout the depth of the boundary layer (Figure 10c,d,g). Beyond a 40-km radius, $\overline{\theta}_e$ decreases in the upper boundary layer,
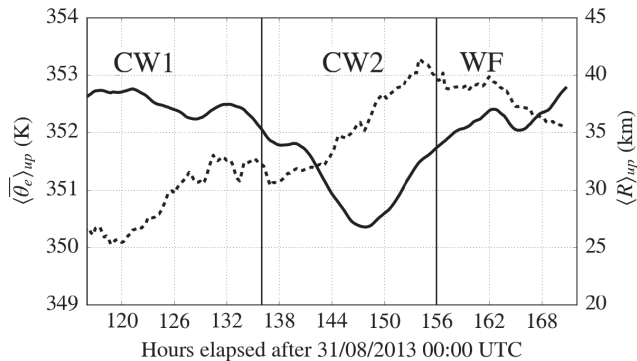
FIGURE 11 Time series of the azimuthal-mean equivalent potential temperature at 780 m averaged over all radii where vertical velocity exceeds $0.25\,\mathrm{m\cdot s^{-1}}$, $\langle\overline{\theta_e}\rangle_{up}$, and the mean updraught radius where the vertical velocity exceeds $0.25\,\mathrm{m\cdot s^{-1}}$, $\langle R\rangle_{up}$. Both variables are shown as a 3-hr running mean

as shown by the descending dark blue region of low $\overline{\theta_e}$. Conversely, the increase in average surface latent heat flux during the latter stage of CW2 and WF is accompanied by an increase in $\overline{\theta_e}$ inside a 40-km radius throughout the depth of the boundary layer. At radii beyond 40 km, $\overline{\theta_e}$ continues to decrease (Figure 10d–g).

Figure 11 shows the same $\overline{\theta_e}$ in Figure 10g averaged over all radii where the vertical velocity exceeds $0.25\,\mathrm{m\cdot s^{-1}}$, $\langle\overline{\theta_e}\rangle_{up}$, as well as the mean radius of this updraught region, $\langle R\rangle_{up}$. During CW1, $\langle\overline{\theta_e}\rangle_{up}$ decreases on account of a negative radial gradient in $\overline{\theta_e}$ and an increasing $\langle R\rangle_{up}$. The transient decrease in $\overline{\theta_e}$ inside a 20-km radius does not have a large effect on $\langle\overline{\theta_e}\rangle_{up}$, because the corresponding updraught extends approximately from 15- to 40-km radius. During CW2, $\langle\overline{\theta_e}\rangle_{up}$ decreases faster than in CW1 on account of both an increasing $\langle R\rangle_{up}$ and the local decrease in $\overline{\theta_e}$ inside a 40-km radius. Conversely, $\langle\overline{\theta_e}\rangle_{up}$ increases during the latter stage of CW2 and WF, due to both the local increase in $\overline{\theta_e}$ inside a 40-km radius and, from the end of CW2 onwards, a decreasing $\langle R\rangle_{up}$.

Besides decreasing surface latent heat flux, vortex-tilt-induced downdraughts in a large vertical wind shear environment can bring low-θ_e air into the boundary layer at radii beyond the eyewall updraught and reduce θ_e there (Molinari *et al.*, 2013; Zhang *et al.*, 2017; Wadler *et al.*, 2018). Riemer *et al.* (2010) show that the pattern of anomalously low-θ_e air is inherently asymmetric and that the downward flux of low-θ_e air increases with increasing vertical wind shear and decreasing intensity. To quantify the flushing of low-θ_e air into the boundary layer, Riemer *et al.* (2010) examine the downward flux of θ_e, *DFX*, which they define as

$$DFX = w_-\theta'_e,\qquad(2)$$

where w_- is the vertical velocity in the downdraught region and θ'_e is the deviation of local θ_e from the azimuthal mean, $\overline{\theta_e}$. Regions of downdraught with anomalously low θ_e are positive. Note that regions of updraught with anomalously high θ_e will also yield positive values of *DFX*.

Figure 12 shows the *DFX* and the vertical velocity at the top of the boundary layer at 780 m height.[2] The positive values of *DFX* are found mainly in the eyewall updraught region, corresponding to ascending air parcels with anomalously high θ_e. While positive *DFX* values in the downdraught regions widely exceed $0.5\,\mathrm{K\cdot s^{-1}}$ in Riemer *et al.* (2010) for a comparable wind shear of $10\,\mathrm{m\cdot s^{-1}}$, they are weaker than $0.5\,\mathrm{K\cdot s^{-1}}$ in Figure 12, with the exception of Figure 12a at 92 hr.

The small downward flux of low-θ_e air suggests that the flushing of low θ_e is less important for the decrease in $\langle\overline{\theta_e}\rangle_{up}$ during CW1 and CW2 than the change in surface latent heat fluxes. The low $\overline{\theta_e}$ contours that descend into the boundary layer (Figure 10c–f) are instead likely to be due to drier environmental air as the tropical cyclone moves to higher latitudes (not shown).

The foregoing analysis points to an important role played by changes in the surface latent heat flux in determining the accompanying changes in $\overline{\theta_e}$. Both the changes in $\overline{\theta_e}$ and the mean radius of the boundary-layer updraught determine the changes in buoyancy of ascending air parcels at the top of the boundary layer, which are reflected in $\langle\overline{\theta_e}\rangle_{up}$.

4.5 | Vertical mass flux

While the equivalent potential temperature of the air parcels in the boundary layer determines their buoyancy, the ability of the eyewall updraught to accept ascending boundary-layer air depends on the difference between the vertical mass flux within the eyewall updraught and its base at the top of the boundary layer. Figure 13 displays the vertical mass flux averaged over radii between zero and 60 km for heights of 780 m, $\overline{\rho w}_{780m}$, and 5 km, $\overline{\rho w}_{5km}$, respectively. The eyewall updraught at 5 km height lies inside a 60-km radius, as shown by the $0.5\,\mathrm{m\cdot s^{-1}}$ contour in Figure 5. During RI, $\overline{\rho w}_{780m}$ and $\overline{\rho w}_{5km}$ increase. The increasing gap between $\overline{\rho w}_{780m}$ and $\overline{\rho w}_{5km}$ shows that the strengthening convection in the eyewall updraught is increasingly able to accept vertical mass flux from the boundary layer. During CW1, $\overline{\rho w}_{780m}$ and $\overline{\rho w}_{5km}$ remain relatively constant. During CW2, $\overline{\rho w}_{5km}$ falls rapidly at first and then continues to decrease more gradually.

---

[2]Note that Riemer *et al.* (2010) calculate the *DFX* at the top of the inflow layer at 1.5 km, and not at the top of the boundary layer.
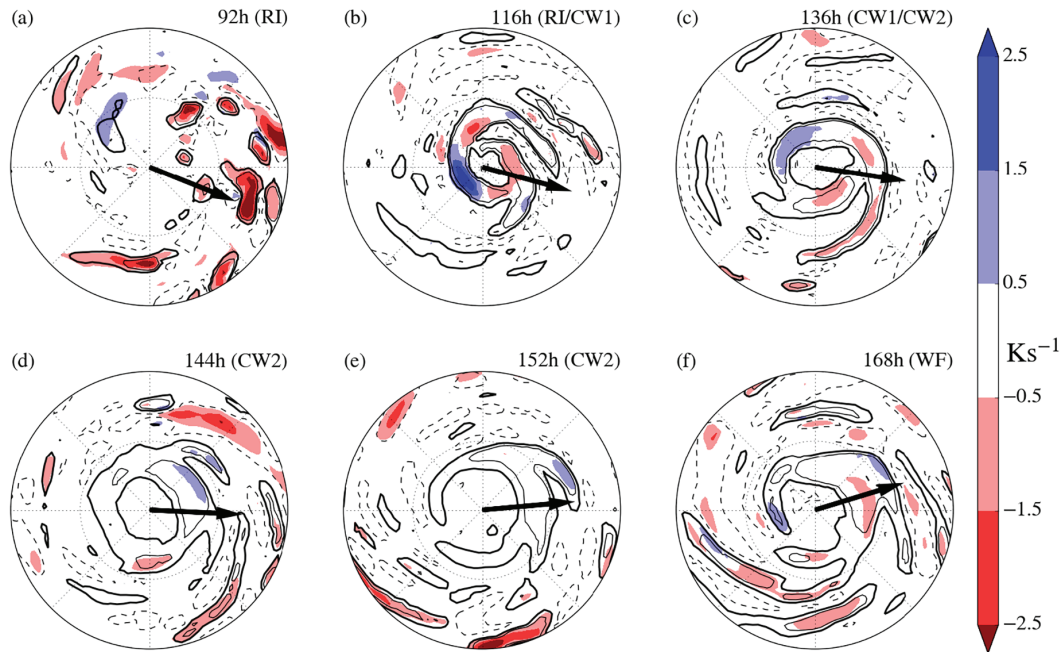
FIGURE 12 Instantaneous horizontal snapshots of the downward flux of θ_e', DFX (blue and red shading), and vertical velocity (black contours) at a height of 780 m at (a) 92, (b) 116, (c) 136, (d) 144, (e) 152, and (f) 168 hr after August 31, 2013, 0000 UTC. Contours are displayed for vertical velocities of −0.1 (dashed), 0.25 (thick), and 0.5 m·s^{-1} (thin). The direction of the vertical wind shear is indicated by the arrow. Radial grid lines are displayed for 50 and 100 km
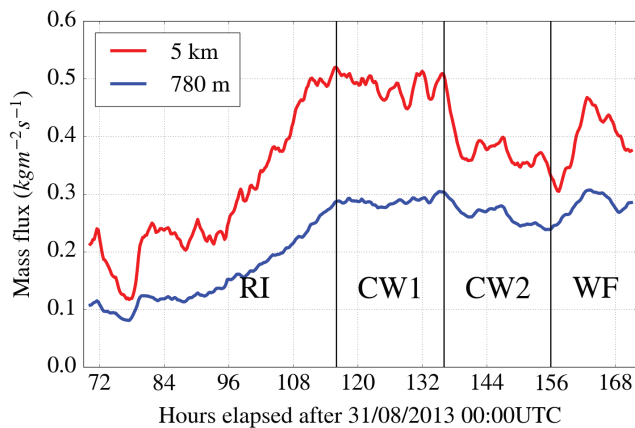

FIGURE 13 Upward mass fluxes averaged within a radius of 60 km are shown as a 3-hr running mean for heights of 780 m (blue) and 5 km (red)

A similar rapid fall is not seen for $\overline{\rho w}_{780m}$, which decreases gradually throughout CW2. This discrepancy shows that, while deep convection weakens substantially in the eyewall updraught, boundary-layer convergence remains relatively strong. Consequently, the deep convection in the eyewall updraught is less able to ventilate the vertical mass flux from the boundary layer. As a result, there is substantial weakening of the inflow into the eyewall updraught from above the boundary layer, as seen in Section 4.6. During the latter stage of CW2 and WF, $\overline{\rho w}_{780m}$ and $\overline{\rho w}_{5km}$

experience a sharp increase and peak before decreasing again, which is consistent with a substantial strengthening of deep convection (Figure 4e,f).

4.6 | Updraught and inflow

The difference between the vertical mass flux in the eyewall updraught at around 5 km height, where the vertical velocities are largest, and at its base at the top of the boundary layer determines the strength of the radial inflow above the boundary layer. The azimuthal-mean inflow and updraught for the lowermost 4 km are displayed in Figure 14. During CW1 and CW2, the inflow strengthens between 92 and 116 hr (Figure 14a,b). During the mature phase, the inflows above and below 1 km do not weaken in unison. Comparing the 1 and 2 m·s^{-1} contours in Figure 14b and c reveals a weakening of the inflow inside a 100-km radius during CW1. In contrast, the 5 and 10 m·s^{-1} contours show that the inflow in the lowermost 1 km remains relatively constant. The inflow also reflects the radially outward movement of the eyewall updraught. From Figure 14c and d, it is evident that the inflow inside a 100-km radius continues to weaken above 1 km in CW2, while the inflow below 1 km remains relatively constant.

As the eyewall moves radially inwards during WF, the inflow strengthens both above and below 1 km within the
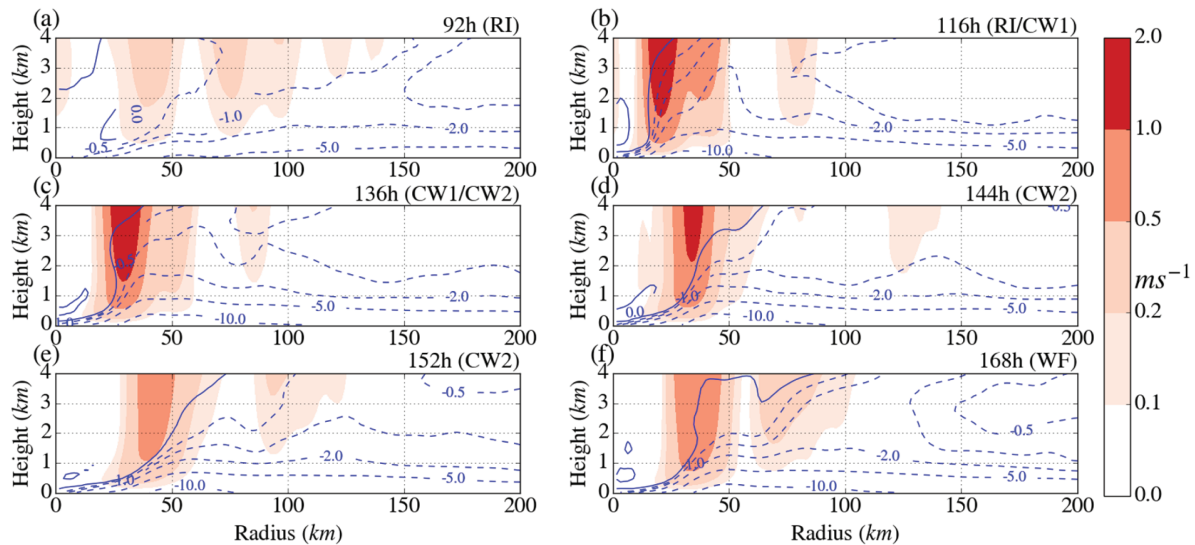
FIGURE 14 Azimuthal-mean of secondary circulation shown as a 3-hr running mean for 92, 116, 136, 144, 152, and 168 hr after August 31, 2018, 0000 UTC. The red shading indicates the magnitude of vertical velocity. Inflow contours are displayed as blue lines, corresponding to (0.0, 0.5, 1.0, 2.0, 5.0, 10.0) m·s^{-1}

innermost 100 km, as shown by the 1, 5, and 10 m·s^{-1} contours (Figure 14e,f). The strengthening inflow indicated by the 1 m·s^{-1} contour coincides with a second updraught region that is weaker than the primary updraught region and is located between radii of 50 and 100 km. This second updraught region is associated with a spiral band rather than a secondary eyewall, as seen from the plane-view plot of vertical velocity in Figure 4e,f.

4.7 | Absolute angular momentum

The changing radial inflow in a vertical layer above the boundary layer leads to changes in the radial advection of absolute angular momentum (M) surfaces. Figure 15 displays a Hovmöller plot of the M-surfaces and the vertical velocity at the top of the boundary layer. During RI, the M contours move radially inwards over time for all radii inside 100 km. During CW1, the M contours inside the updraught region (characterised by a vertical velocity greater than 0.25 m·s^{-1}) move radially outwards, as seen from the 1×10^6 m^2·s^{-1} and 1.5×10^6 m^2·s^{-1} contours. The M contours at larger radii continue to move radially inwards in the intervening period. During CW2, in contrast, all the displayed M contours move outwards over time. Although the radial flow beyond the eyewall updraught region is directed inwards during CW2, the vertical advection of low M from below leads to the displayed M contours moving outwards. During the latter stage of CW2 and WF, the displayed M contours move inwards inside a radius of 100 km.
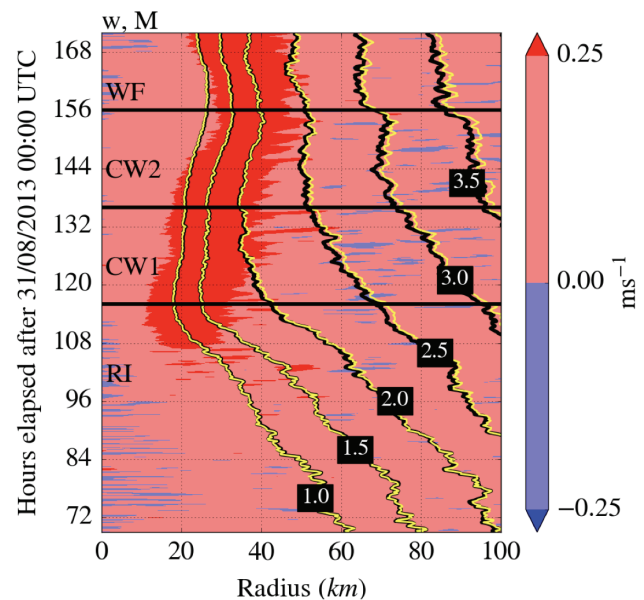

FIGURE 15 Hovmöller plot of angular momentum (M) and vertical velocity. The M contours at heights of 780 and 620 m are shown as black and yellow lines, respectively. The contours are displayed for (1.0, 1.5, 2.0, 2.5, 3.0, 3.5) $\times 10^6$ m^2·s^{-1}. The shading indicates the vertical velocity at 780 m according to the color bar

4.8 | Discussion

The foregoing analysis allows us to understand the evolution of the azimuthal-mean structure and intensity of the tropical cyclone during the mature phase in terms of the conceptual framework outlined in Section 3. In the

following, we synthesise the foregoing analysis and discuss the change in azimuthal-mean structure and intensity separately for the initial period of decay, the latter period of decay, and the period of reintensification. Comparing and contrasting the three different periods offers an insight into the importance of boundary-layer dynamics and air–sea coupling. The schematic in Figure 1 outlining the conceptual framework used for the preceding analysis may prove useful in the following discussion.

During CW1, the wind-stress-induced sea-surface cooling leads to a decrease in the SST averaged within the radius of maximum near-surface wind. The decrease in SST and the accompanying decrease in the moisture disequilibrium at the air–sea interface, Δq, dominate the overall decrease in the average surface latent heat flux within the same radius. The average surface latent heat flux reaches a local minimum, which is accompanied by a transient decrease in the azimuthal-mean equivalent potential temperature at the top of the boundary layer, $\overline{\theta_e}$, inside a 20-km radius. However, the transient decrease in $\overline{\theta_e}$ does not have a large influence on the mean $\overline{\theta_e}$ of air ascending into the eyewall updraught at the top of the boundary layer that is characterised by vertical velocities exceeding $0.25\,\mathrm{m\cdot s^{-1}}$, $\langle\overline{\theta_e}\rangle_{up}$. This is because the corresponding updraught region at the top of the boundary layer extends from 15–40 km radius. Hence, $\langle\overline{\theta_e}\rangle_{up}$ is not appreciably affected by the decrease in the average surface latent heat flux. During CW1, the mean radius of the eyewall updraught increases on account of nonlinear boundary-layer dynamics in the presence of the expanding outer circulation. As the mean radius of the updraught increases, $\langle\overline{\theta_e}\rangle_{up}$ decreases. The decreasing $\langle\overline{\theta_e}\rangle_{up}$ reduces the local buoyancy of air parcels in the eyewall updraught, which leads to a decrease in the vertical velocity in the eyewall updraught. While the vertical velocity decreases at a height of 5 km, which is in the middle troposphere, the average vertical mass flux remains steady[3] within a radius of 60 km, which includes the outward-moving eyewall updraught. Since the difference between the vertical mass flux of the eyewall updraught in the middle troposphere and at the base of the eyewall updraught remains large, the eyewall updraught is more than able to accept the ascending boundary-layer air and produce a strong radial inflow in a vertical layer above the boundary layer at radii beyond the eyewall updraught. In turn, the radial inflow draws absolute angular momentum (M) surfaces, leading to a local increase in the tangential wind speed. Because the tangential wind speed above the boundary layer remains in gradient-wind balance to a

good approximation (not shown), the local increase in the tangential wind speed increases the local radial pressure gradient, which is transmitted essentially unchanged into the boundary layer. The increase in the radial pressure gradient in the boundary layer changes the net radial force in the boundary layer at radii beyond the eyewall updraught. As shown by Kilroy et al. (2016), the expanding outer circulation leads to an increase in the mean radius of the air ascending into the eyewall updraught through nonlinear boundary-layer dynamics.

During CW2, the decreasing translational speed of the tropical cyclone leads to stronger sea-surface cooling and a further decrease in the average SST. As in CW1, the decrease in the average SST and the accompanying decrease in Δq during CW2 are primarily responsible for the decrease in the average surface latent heat flux, all of which reach a global minimum for the RI phase and the mature phase. The decrease in the surface latent heat flux is accompanied by a decrease in $\overline{\theta_e}$ at the top of the boundary layer inside a 100-km radius. Consequently, $\langle\overline{\theta_e}\rangle_{up}$ decreases faster than in CW1 on account of both the local decrease in $\overline{\theta_e}$ and the increasing mean radius of the ascending air controlled by the expanding outer circulation. As before, the decreasing $\langle\overline{\theta_e}\rangle_{up}$ reduces the local buoyancy and the vertical velocity in the eyewall updraught. In contrast to CW1, the decrease in vertical velocity is accompanied by a decrease in the vertical mass flux in the eyewall updraught. Nevertheless, the vertical mass flux in the eyewall updraught remains larger than that at its base. Hence, the eyewall updraught is still able to accept all the ascending boundary-layer air, although the radial inflow weakens in a vertical layer above the boundary layer at radii beyond the eyewall updraught. The weaker radial inflow, combined with the vertical advection of low M from within the boundary layer, leads to M-surfaces moving radially outwards above the boundary layer at radii beyond the eyewall updraught up to 100-km radius. Within this radial interval, the tangential wind speed at the top of the boundary layer decreases along with the radial pressure gradient transmitted into the boundary layer. The decrease in the radial pressure gradient changes the net radial force in the boundary layer. Through nonlinear boundary-layer dynamics, the changes in the net radial force, together with the expanding outer circulation, lead to an accelerated increase in the mean radius of air ascending into the eyewall updraught compared with CW1.

During the latter stage of CW2 and WF, the foregoing tendencies are reversed. The subsurface warm-core eddy reduces the strength of sea-surface cooling and the average SST increases. The increase in average SST and the accompanying increase in Δq are primarily responsible for the increase in average surface latent heat flux. The increase in the surface latent heat flux is accompanied by

---

[3]Since the areal extent of the eyewall updraught increases, decreasing vertical velocity does not necessarily equate to a decreasing vertical mass flux.

an increase in $\overline{\theta_e}$ at the top of the boundary layer at radii inside 40 km. The value of $\langle\overline{\theta_e}\rangle_{up}$ increases because of both the local increase in $\overline{\theta_e}$ and the decreasing mean radius of the updraught, leading to an increase in the local buoyancy and the vertical velocity in the eyewall updraught. The increase in vertical velocity is accompanied by a sharp increase in the vertical mass flux in the eyewall updraught. Since the difference between the vertical mass flux within and at the base of the inward-moving eyewall updraught increases, the eyewall updraught is more able to accept ascending boundary-layer air than during the decay in CW2. As a result, the radial inflow strengthens above the boundary layer and M-surfaces are drawn inwards at radii beyond the eyewall updraught. Correspondingly, the tangential wind speed at the top of the boundary layer increases along with the radial pressure gradient transmitted into the boundary layer at radii beyond the eyewall updraught. Again, through nonlinear boundary-layer dynamics, the strengthening outer circulation leads to a decrease in the mean radius of air ascending into the eyewall updraught, although a part of this decrease may be associated with local suction effects of the increasing vertical mass flux, which are not captured by boundary-layer dynamics.

The outward-moving eyewall updraught in CW1 resembles the simulation in Kilroy *et al.* (2016) with constant SST, because the decrease in average surface latent heat flux does not have an appreciable effect on the thermodynamics of air ascending from the boundary layer into the eyewall updraught, captured by $\langle\overline{\theta_e}\rangle_{up}$. In CW2, by contrast, the decrease in $\langle\overline{\theta_e}\rangle_{up}$ cannot be explained without air–sea coupling. Air–sea coupling is also crucial during the latter stage of CW2 and WF, where the increase in the average surface latent heat flux is accompanied by an increase in $\langle\overline{\theta_e}\rangle_{up}$ and a burst in eyewall convection.

The foregoing discussion shows that the changes in SST and surface latent heat flux alone do not fully explain the changes in tropical cyclone intensity. Instead, it is necessary to consider both air–sea interactions and boundary-layer dynamics in order to acquire a complete picture of the changes in the azimuthal-mean structure and intensity of the simulated tropical cyclone.

Although repeating the coupled simulation at higher resolution may improve the robustness of the foregoing results, there are several reasons to believe that the qualitative behaviour described above would not change. Firstly, Fierro *et al.* (2009) found that the amplitudes of low-wavenumber asymmetries decrease with finer grid spacing from 5 to 1 km, suggesting that azimuthal-mean analysis would be appropriate down to at least a grid spacing of 1 km. Secondly, the most severe impact on the above results is likely to be connected to the diffusivity of

the boundary-layer scheme. In models with overly diffusive boundary-layer schemes, the boundary-layer spin-up mechanism tends to be weaker (Smith and Thomsen, 2010). This is because the boundary-layer depth scales with the square root of the eddy diffusivity (Smith, 1968). Since deeper boundary layers tend to have a weaker inflow, the eddy diffusivity affects the inward advection of M-surfaces in the boundary layer. Nevertheless, the preceding analysis shows good agreement with the conceptual framework and this is unlikely to change with a less diffusive boundary-layer scheme. This agreement highlights the importance of understanding the individual processes within the conceptual framework, which recognises the role of boundary-layer dynamics and air–sea coupling for changes in tropical cyclone intensity.

5 | THE ROLE OF BOUNDARY-LAYER DYNAMICS FOR INTENSITY

As outlined in the conceptual framework (Section 3), the expanding outer circulation determines the change in both the boundary-layer convergence and the radius of forced ascent through the boundary-layer dynamics. In Section 4, we articulated how these aspects of boundary-layer dynamics influence the decay and reintensification of a tropical cyclone simulated in the coupled atmosphere–ocean ICON model. However, we did not provide evidence for the expanding outer circulation controlling the increase in mean updraught radius at the top of the boundary layer on account of boundary-layer dynamics as the tropical cyclone decays. Nor did we demonstrate a similar control when the mean updraught radius decreases during reintensification.

In this section, we follow Kilroy *et al.* (2016) and compare the ICON simulation with a steady-state slab boundary-layer model (Smith, 2003). By indicating the change in the radius of forced ascent in the presence of an expanding circulation, the comparison with the slab boundary layer provides an insight as to whether the expanding circulation is controlling the change in the radius of forced ascent in the ICON simulation.

5.1 | Slab boundary-layer model

The slab boundary-layer model solves for the radial velocity, $u_b(r)$, and tangential velocity, $v_b(r)$, in the boundary layer as a function of radius, r. The equations governing

the steady-state slab boundary-layer model used here are derived from the momentum and continuity equations (see Appendix). Therefore, the solution is based on dynamical considerations only; surface latent heat flux and inner-core convection in the eyewall are not included explicitly. Nonlinear terms, which are particularly large and cannot be neglected in the boundary layer, are retained in the momentum equations (Vogl and Smith, 2009). A steady-state model is appropriate here, because the boundary layer is thin and reacts to changes in the radial pressure gradient on short time-scales (Kilroy *et al.*, 2016).

The boundary conditions for the slab boundary-layer model are the radial pressure gradient at the top of the boundary layer at height h and the frictional drag at the sea surface. We neglect the momentum flux into the boundary layer at h due to vertical diffusion, which is assumed to be small compared with the surface term. The radial pressure gradient at h is derived from the tangential velocity, assumed to be in gradient wind balance, and is transmitted into the slab boundary layer. The surface momentum flux is derived from the standard bulk aerodynamic formula and depends on the wind speed and a drag coefficient, C_D. Density does not enter into the equations, because the fluid is assumed to be homogeneous.

For reasons outlined in Section 4.1, we prescribe a fixed h of 780 m for the slab boundary-layer model. The tangential velocity from the corresponding vertical level is then used for the upper boundary condition. The choice of 780 m is also consistent with the assumption of gradient wind balance at h, which is satisfied during the mature phase in the ICON simulation to a good approximation (not shown).

We implement a function for C_D in the slab boundary-layer model that is compatible with observations (Black *et al.*, 2007) and is given by

$$C_D = C_{D0} + C_{D1}\left(1 - e^{-\alpha_d v_g}\right).$$

The gradient wind speed at the top of the boundary layer is denoted by v_g. When v_g is zero, C_D is equal to C_{D0}. For small v_g, C_D approximates a linear function of v_g. For large v_g, C_D approaches $C_{D0} + C_{D1}$ asymptotically. The coefficients C_{D0}, C_{D1}, and α_d are set to 0.7×10^{-3}, 1.4×10^{-3}, and 5.5×10^{-2}, respectively. These coefficients are chosen to fit C_D in the ICON model as closely as possible. With a view to keeping the model simple, we accept that an exact fit is not possible, because C_D in the ICON model is a more complicated function that is not only dependent on wind speed, but also consistent with the model's turbulence scheme.
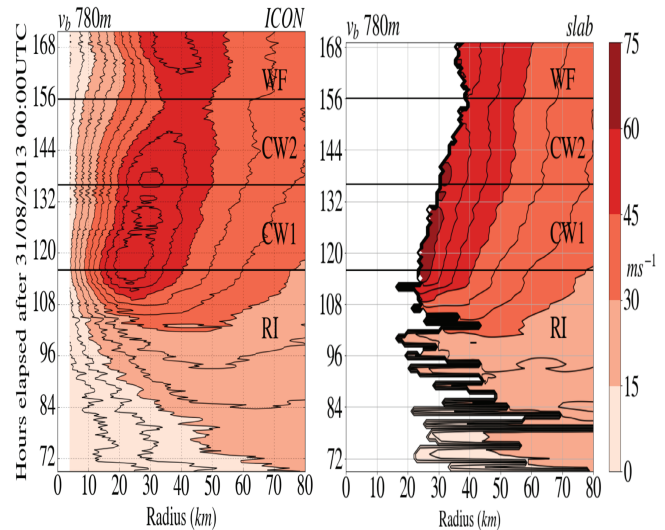

FIGURE 16   The tangential velocity in the boundary layer, v_b, is displayed as a Hovmöller plot for the ICON (left) and slab boundary-layer model (right). For the ICON simulation, v_b represents a vertical average of tangential velocity over the lower 780 m in the atmosphere

5.2 | Results from the slab boundary-layer model

To facilitate a fair comparison with the slab boundary-layer model, the tangential and radial velocity in the ICON simulation are averaged over the lowermost 780 m. As shown in Figure 16, the slab boundary-layer model captures the outward shift of v_b contours during CW1 and CW2. The slopes of the v_b contours in the slab boundary-layer model are in good agreement with the ICON simulation. For WF, the slab boundary layer correctly predicts that the v_b contours within a radius of 50 km no longer move outwards. However, while the inner edge of the solution moves inward, the slab boundary-layer model is unable to capture the full extent of the contraction in the ICON simulation; the v_b contours between 40 and 60 km do not move inwards. Note that a comparison is not possible at small radii, because the slab boundary-layer solution breaks down when u_b goes to zero, shown by the cut-off.

The comparison for u_b is shown in Figure 17. Although u_b is consistently larger in the slab boundary-layer model, the slab boundary-layer model correctly predicts the expansion of u_b contours during CW1 and CW2 followed by the contraction in WF. Moreover, there is good agreement with the strengthening between the latter half of CW2 and WF.
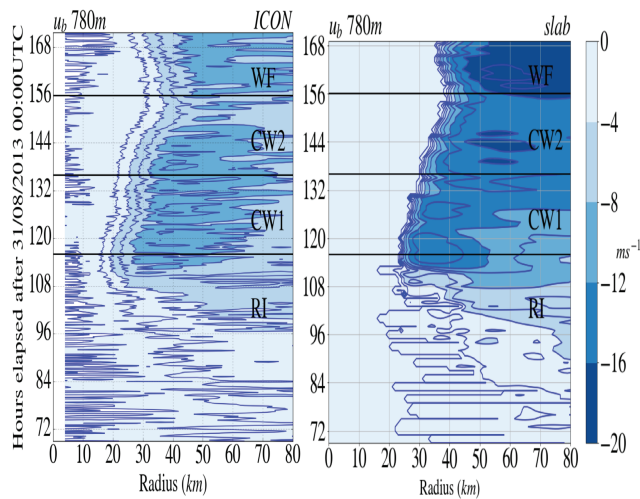
FIGURE 17 The radial velocity in the boundary layer, u_b, is displayed as a Hovmöller plot for the ICON simulation (left) and slab boundary-layer model (right). For the ICON simulation, u_b represents a vertical average of tangential velocity over the lower 780 m in the atmosphere

5.3 | Discussion of results from the slab boundary-layer model

One cannot expect to avoid quantitative differences when comparing the ICON simulation with the highly idealised slab boundary-layer model. Kepert (2010) showed that the slab boundary-layer model tends to overestimate the inflow strength, which is consistent with our results. At the same time, the weaker boundary-layer flow in the ICON simulation may be linked to excessive vertical diffusion in the ICON model (Zhang *et al.*, 2010). An indication of excessive vertical diffusion is the relatively weak vertical gradient of inflow in the boundary layer (not shown) (Gopalakrishnan *et al.*, 2013). Combined with the sensitivity of the slab boundary-layer model to h, as well as the lack of consensus on the definition of h, it does not make sense to provide an interpretation of small quantitative differences for our purposes (Zhang *et al.*, 2011).

Despite its limitations, the slab boundary-layer model provides an important qualitative insight into the change in the radius of forced ascent at the top of the boundary layer, because its governing equations are parabolic. Information in parabolic equations flows in the direction of the physical flow, which is radially inwards in the slab boundary-layer model. Consequently, u_b and v_b at a given radius do not depend on the solution at smaller radii. For this reason, the slab boundary-layer model does not include the convective suction effect described in Section 3.

The results for CW1 and CW2 are similar to the findings in Kilroy *et al.* (2016) for a decaying tropical cyclone

and constant SST, where the slab boundary-layer model predicted the expansion of the u_b and v_b contours. As with Kilroy *et al.* (2016), the expansion of the u_b and v_b contours show that an increasing radius of forced ascent is being controlled by the expanding outer circulation in the ICON simulation via boundary-layer dynamics.

Similarly to CW1 and CW2, the slab boundary-layer model can predict the contraction of the u_b contours and the innermost v_b contour. Again, the agreement between the ICON simulation and slab boundary layer shows that a decreasing radius of forced ascent is being determined by the expanding outer circulation through boundary-layer dynamics. The inability of the slab boundary-layer model to capture the full extent of the contraction of the v_b contours during WF is likely to be related to the enhanced convective suction effect discussed in Section 4.8.

6 | SUMMARY AND CONCLUSIONS

We examine how the atmospheric boundary layer modulates the intensity of a mature tropical cyclone influenced by a realistic ocean-eddy field in a fully coupled atmosphere–ocean model. To this end, we analyse a tropical cyclone simulated in the ICON model with a global, nonhydrostatic configuration and a horizontal grid spacing of 5 km. After reaching peak intensity, the simulated tropical cyclone experiences a period of decay following the interaction with its cold wake and subsequently reintensifies as it encounters a subsurface, warm-core eddy. The changes in the azimuthal-mean structure and intensity are analysed with the help of a conceptual framework that recognises the importance of boundary-layer dynamics, as well as the role played by air–sea interactions. A key part of the framework is the recognition that the change in the mean radius of updraught at the boundary-layer top is regulated by the expanding outer tangential wind field through boundary-layer dynamics.

Our study shows that the outward movement of the eyewall updraught associated with the cold wake is not due to air–sea interactions alone. During the early decay phase, the decrease in the average equivalent potential temperature of the boundary-layer updraught is related to an increase in the mean radius of the updraught rather than the decreasing SST and surface latent heat flux. However, later in the decay phase the decreasing SST and surface latent heat flux contribute to the decrease in equivalent potential temperature of the boundary-layer updraught. The accompanying decrease in the vertical mass flux in the interior of the eyewall updraught causes the radial inflow above the boundary layer to weaken, which ultimately leads to a more pronounced spin-down than earlier in the decay phase.

Similarly, boundary-layer dynamics and air–sea interactions both play an important role for the inward movement of the eyewall updraught in the reintensification phase, where the tendencies are reversed. The average equivalent potential temperature of the boundary-layer updraught is related to the decrease in the mean radius of the updraught, as well as the increase in local equivalent potential temperature arising from increasing SST and surface latent heat flux. The accompanying increase in vertical mass flux leads to a strengthening radial inflow above the boundary layer and spin-up of the tropical cyclone.

The ability of a steady-state slab boundary-layer model to predict the increase in the radius of forced ascent during the decay phase and, to a lesser extent, the subsequent decrease during reintensification provides evidence for the boundary-layer mechanism, first articulated by Kilroy *et al.* (2016), in a coupled atmosphere–ocean simulation. Namely, that the change in the radius of forced ascent is controlled by the expanding outer circulation on account of nonlinear boundary-layer dynamics. In turn, the change in the radius of forced ascent influences deep convection in the eyewall updraught, which then feeds back on the boundary-layer flow.

In addition, this study highlights another layer of complexity to the coupling between surface latent heat flux, SST, and near-surface wind speed through boundary-layer dynamics. The near-surface wind speed and the change in surface latent heat flux are linked to the boundary-layer flow and depend on whether convergence in the boundary layer is dominated by the nonlinear dynamics of the boundary-layer flow or the suction effect. Thus, any feedback between surface latent heat flux and tropical cyclone intensity in coupled models ultimately involves nonlinear boundary-layer dynamics.

Taken together, the foregoing results show that boundary-layer dynamics should be incorporated into any explanation of changes in tropical cyclone intensity in response to sea-surface cooling in coupled atmosphere–ocean models with a realistic ocean-eddy field.

Further work is required to establish the robustness of these results for various degrees of sea-surface cooling and vertical wind shear. This is because sea-surface cooling tends to be highly asymmetric and vertical wind shear induces strong asymmetries in the tropical cyclone circulation. Such asymmetries are not captured in an axisymmetric framework. The asymmetric downdraughts associated with vertical wind shear and vortex tilt have been shown in previous studies to have a substantial effect on the boundary-layer thermodynamics, but it is not clear how these changes would affect the radius of forced ascent at the top of the boundary layer in a coupled atmosphere–ocean model. Further, recent studies have demonstrated that the sea-surface cooling can lead to the formation of a stable boundary layer over the asymmetric cold wake, which leads to asymmetries in the boundary-layer flow. Again, it is unclear to what extent this asymmetric flow influences the radius of forced ascent.

Finally, this is the first study that investigates the effect of a warm-core eddy at depth on the kinematic structure of the tropical cyclone boundary layer with a fully three-dimensional eddy-resolving simulation. While the warm-core eddy is able to sustain a large surface latent heat flux and reduce sea-surface cooling due to large ocean heat content, the degree of reintensification is inextricably linked to the decreasing radius of forced ascent and the accompanying changes in the kinematic and thermodynamic structure of the boundary layer. Conversely, our results suggest that boundary-layer dynamics play an important role in sea-surface cooling in coupled atmosphere–ocean simulations. Specifically, understanding the link between the outer circulation and radius of forced ascent through boundary-layer dynamics may improve predictions of tropical cyclone size, which is an important factor for sea-surface cooling.

AUTHOR CONTRIBUTIONS

Arjun U. Kumar: conceptualization; formal analysis; investigation; methodology; visualization; writing – original draft; writing – review and editing. **Nils Brüggemann:** conceptualization; formal analysis; investigation; methodology; project administration; resources; supervision; writing – review and editing. **Roger K. Smith:** conceptualization; formal analysis; investigation;

methodology; supervision; writing – review and editing. **Jochem Marotzke:** conceptualization; formal analysis; funding acquisition; investigation; methodology; project administration; resources; supervision; writing – review and editing.

ORCID
Arjun U. Kumar https://orcid.org/0000-0002-3058-5105

REFERENCES

Abarca, S.F., Montgomery, M.T. and McWilliams, J.C. (2015) The azimuthally averaged boundary layer structure of a numerically simulated major hurricane. *Journal of Advances in Modeling Earth Systems*, 7(3), 1207–1219. https://doi.org/10.1002/2015MS000457.

Balaguru, K., Foltz, G.R., Leung, L.R., Hagos, S.M. and Judi, D.R. (2018) On the use of ocean dynamic temperature for hurricane intensity forecasting. *Weather and Forecasting*, 33(2), 411–418. https://doi.org/10.1175/waf-d-17-0143.1.

Bender, M.A. and Ginis, I. (2000) Real-case simulations of hurricane–ocean interaction using a high-resolution coupled model: effects on hurricane intensity. *Monthly Weather Review*, 128(4), 917–946. https://doi.org/10.1175/1520-0493(2000)128<0917:RCSOHO>2.0.CO;2.

Bender, M.A., Ginis, I. and Kurihara, Y. (1993) Numerical simulations of tropical cyclone–ocean interaction with a high-resolution coupled model. *Journal of Geophysical Research*, 98(D12), 23 245–23 263. https://doi.org/10.1029/93jd02370.

Black, P.G., D'Asaro, E.A., Drennan, W.M., French, J.R., Niiler, P.P., Sanford, T.B., Terrill, E.J., Walsh, E.J. and Zhang, J.A. (2007) Air–sea exchange in hurricanes: synthesis of observations from the coupled boundary-layer air–sea transfer experiment. *Bulletin of the American Meteorological Society*, 88(3), 357–374. https://doi.org/10.1175/BAMS-88-3-357.

Bryan, G.H. and Rotunno, R. (2009) The maximum intensity of tropical cyclones in axisymmetric numerical model simulations. *Monthly Weather Review*, 137(6), 1770–1789. https://doi.org/10.1175/2008MWR2709.1.

Chang, S.W. and Anthes, R.A. (1978) Numerical simulations of the ocean's nonlinear, baroclinic response to translating hurricanes. *Journal of Physical Oceanography*, 8(3), 468–480. https://doi.org/10.1175/1520-0485(1978)008<0468:NSOTON>2.0.CO;2.

Chang, S.W. and Anthes, R.A. (1979) The mutual response of the tropical cyclone and the ocean. *Journal of Physical Oceanography*, 9(1), 128–135. https://doi.org/10.1175/1520-0485(1979)009<0128:tmrott>2.0.co;2.

Chen, S., Campbell, T.J., Jin, H., Gaberšek, S., Hodur, R.M. and Martin, P. (2010) Effect of two-way air–sea coupling in high and low wind speed regimes. *Monthly Weather Review*, 138(9), 3579–3602. https://doi.org/10.1175/2009MWR3119.1.

Chen, S., Elsberry, R.L. and Harr, P.A. (2017) Modeling interaction of a tropical cyclone with its cold wake. *Journal of the Atmospheric Sciences*, 74(12), 3981–4001. https://doi.org/10.1175/JAS-D-16-0246.1.

Cione, J.J. and Uhlhorn, E.W. (2003) Sea surface temperature variability in hurricanes: implications with respect to intensity change. *Monthly Weather Review*, 131(8), 1783–1796. https://doi.org/10.1175//2562.1.

Dee, D.P., Uppala, S.M., Simmons, A.J., Berrisford, P., Poli, P., Kobayashi, S., Andrae, U., Balmaseda, M.A., Balsamo, G., Bauer, P., Bechtold, P., Beljaars, A.C.M., van de Berg, L., Bidlot, J., Bormann, N., Delsol, C., Dragani, R., Fuentes, M., Geer, A.J., Haimberger, L., Healy, S.B., Hersbach, H., Hólm, E.V., Isaksen, L., Kållberg, P., Köhler, M., Matricardi, M., McNally, A.P., Monge-Sanz, B.M., Morcrette, J.J., Park, B.K., Peubey, C., de Rosnay, P., Tavolato, C., Thépaut, J.N. and Vitart, F. (2011) The ERA–Interim reanalysis: configuration and performance of the data assimilation system. *Quarterly Journal of the Royal Meteorological Society*, 137(656), 553–597. https://doi.org/10.1002/qj.828.

Emanuel, K.A. (1986) An air–sea interaction theory for tropical cyclones. Part I: steady-state maintenance. *Journal of the Atmospheric Sciences*, 43(6), 585–605. https://doi.org/10.1175/1520-0469(1986)043<0585:AASITF>2.0.CO;2.

Emanuel, K.A. (1989) The finite-amplitude nature of tropical cyclogenesis. *Journal of the Atmospheric Sciences*, 46(22), 3431–3456. https://doi.org/10.1175/1520-0469(1989)046<3431:TFANOT>2.0.CO;2.

Emanuel, K.A. (1995) Sensitivity of tropical cyclones to surface exchange coefficients and a revised steady-state model incorporating eye dynamics. *Journal of the Atmospheric Sciences*, 52(22), 3969–3976. https://doi.org/10.1175/1520-0469(1995)052<3969:SOTCTS>2.0.CO;2.

Emanuel, K.A. (1997) Some aspects of hurricane inner-core dynamics and energetics. *Journal of the Atmospheric Sciences*, 54(8), 1014–1026. https://doi.org/10.1175/1520-0469(1997)054<1014:SAOHIC>2.0.CO;2.

Emanuel, K.A. (1999) Thermodynamic control of hurricane intensity. *Nature*, 401, 665–669. https://doi.org/10.1038/44326.

Emanuel, K.A. (2013) Downscaling CMIP5 climate models shows increased tropical cyclone activity over the 21st century. *Proceedings of the National Academy of Sciences of the United States of America*, 110(30), 12 219–12 224.

Fierro, A.O., Rogers, R.F., Marks, F.D. and Nolan, D.S. (2009) The impact of horizontal grid spacing on the microphysical and kinematic structures of strong tropical cyclones simulated with the WRF–ARW model. *Monthly Weather Review*, 137(11), 3717–3743. https://doi.org/10.1175/2009mwr2946.1.

Gill, A.E. (1984) On the behavior of internal waves in the wakes of storms. *Journal of Physical Oceanography*, 14, 1129–1151.

Giorgetta, M.A., Brokopf, R., Crueger, T., Esch, M., Fiedler, S., Helmert, J., Hohenegger, C., Kornblueh, L., Köhler, M., Manzini, E., Mauritsen, T., Nam, C., Raddatz, T., Rast, S., Reinert, D., Sakradzija, M., Schmidt, H., Schneck, R., Schnur, R., Silvers, L., Wan, H., Zängl, G. and Stevens, B. (2018) ICON-A, the atmosphere component of the ICON earth system model: I. model description. *Journal of Advances in Modeling Earth Systems*, 10(7), 1613–1637. https://doi.org/10.1029/2017MS001242.

Gopalakrishnan, S.G., Marks, F., Zhang, J.A., Zhang, X., Bao, J.W. and Tallapragada, V. (2013) A study of the impacts of vertical diffusion on the structure and intensity of the tropical cyclones using the high-resolution HWRF system. *Journal of the Atmospheric Sciences*, 70(2), 524–541. https://doi.org/10.1175/JAS-D-11-0340.1.

Guo, T., Sun, Y., Liu, L. and Zhong, Z. (2020) The impact of storm-induced SST cooling on storm size and destructiveness: results from atmosphere–ocean coupled simulations. *Journal*

of *Meteorological Research*, 34(5), 1068–1081. https://doi.org/10.1007/s13351-020-0001-2.

Houze, R.A. (2010) Clouds in tropical cyclones. *Monthly Weather Review*, 138(2), 293–344. https://doi.org/10.1175/2009MWR2989.1.

Jaimes, B. and Shay, L.K. (2009) Mixed layer cooling in mesoscale oceanic eddies during hurricanes Katrina and Rita. *Monthly Weather Review*, 137(12), 4188–4207. https://doi.org/10.1175/2009MWR2849.1.

Jaimes, B., Shay, L.K. and Brewster, J.K. (2016) Observed air–sea interactions in tropical cyclone Isaac over loop current mesoscale eddy features. *Dynamics of Atmospheres and Oceans*, 76, 306–324. https://doi.org/10.1016/j.dynatmoce.2016.03.001.

Jaimes, B., Shay, L.K. and Uhlhorn, E.W. (2015) Enthalpy and momentum fluxes during hurricane Earl relative to underlying ocean features. *Monthly Weather Review*, 143(1), 111–131. https://doi.org/10.1175/MWR-D-13-00277.1.

Jaimes, B., Shay, L.K., Wadler, J.B. and Rudzin, J.E. (2021) On the hyperbolicity of the bulk air–sea heat flux functions: insights into the efficiency of air–sea moisture disequilibrium for tropical cyclone intensification. *Monthly Weather Review*, 149(5), 1517–1534. https://doi.org/10.1175/mwr-d-20-0324.1.

Kaplan, J. and DeMaria, M. (2003) Large-scale characteristics of rapidly intensifying tropical cyclones in the north Atlantic basin. *Weather and Forecasting*, 18(6), 1093–1108. https://doi.org/10.1175/1520-0434(2003)018<1093:lcorit>2.0.co;2.

Kepert, J.D. (2010) Slab- and height-resolving models of the tropical cyclone boundary layer. Part I: comparing the simulations. *Quarterly Journal of the Royal Meteorological Society*, 136(652), 1686–1699. https://doi.org/10.1002/qj.667.

Khain, A. and Ginis, I. (1991) The mutual response of a moving tropical cyclone and the ocean. *Contributions to Atmospheric Physics*, 64, 125–141.

Kilroy, G., Smith, R.K. and Montgomery, M.T. (2016) Why do model tropical cyclones grow progressively in size and decay in intensity after reaching maturity? *Journal of the Atmospheric Sciences*, 73(2), 487–503. https://doi.org/10.1175/JAS-D-15-0157.1.

Korn, P. (2017) Formulation of an unstructured grid model for global ocean dynamics. *Journal of Computational Physics*, 339, 525–552. https://doi.org/10.1016/j.jcp.2017.03.009.

Lee, C.Y. and Chen, S.S. (2014) Stable boundary layer and its impact on tropical cyclone structure in a coupled atmosphere–ocean model. *Monthly Weather Review*, 142(5), 1927–1944. https://doi.org/10.1175/MWR-D-13-00122.1.

Leipper, D.F. and Volgenau, D. (1972) Hurricane heat potential of the Gulf of Mexico. *Journal of Physical Oceanography*, 2(3), 218–224. https://doi.org/10.1175/1520-0485(1972)002<0218:HHPOTG>2.0.CO;2.

Li, D.Y. and Huang, C.Y. (2018) The influences of ocean on intensity of Typhoon Soudelor (2015) as revealed by coupled modeling. *Atmospheric Science Letters*, 20(1), e871. https://doi.org/10.1002/asl.871.

Li, D.Y. and Huang, C.Y. (2019) The influences of ocean on intensity of Typhoon Soudelor (2015) as revealed by coupled modeling. *Atmospheric Science Letters*, 20(1), e871. https://doi.org/10.1002/asl.871.

Lin, I.I., Wu, C.C., Emanuel, K.A., Lee, I.H., Wu, C.R. and Pun, I.F. (2005) The interaction of supertyphoon Maemi (2003) with a warm ocean eddy. *Monthly Weather Review*, 133(9), 2635–2649. https://doi.org/10.1175/MWR3005.1.

Lin, I.I., Wu, C.C., Pun, I.F. and Ko, D.S. (2008) Upper-ocean thermal structure and the western north Pacific category 5 typhoons. Part I: ocean features and the category 5 typhoons' intensification. *Monthly Weather Review*, 136(9), 3288–3306. https://doi.org/10.1175/2008MWR2277.1.

Linden, P.F. (1975) The deepening of a mixed layer in a stratified fluid. *Journal of Fluid Mechanics*, 71(2), 385–405. https://doi.org/10.1017/S0022112075002637.

Ma, Z. (2020) A study of the interaction between typhoon Francisco (2013) and a cold-core eddy. Part I: rapid weakening. *Journal of the Atmospheric Sciences*, 77(1), 355–377. https://doi.org/10.1175/JAS-D-18-0378.1.

Ma, Z., Fei, J., Liu, L., Huang, X. and Cheng, X. (2013) Effects of the cold core eddy on tropical cyclone intensity and structure under idealized air–sea interaction conditions. *Monthly Weather Review*, 141(4), 1285–1303. https://doi.org/10.1175/MWR-D-12-00123.1.

Ma, Z., Fei, J., Liu, L., Huang, X. and Li, Y. (2017) An investigation of the influences of mesoscale ocean eddies on tropical cyclone intensities. *Monthly Weather Review*, 145(4), 1181–1201. https://doi.org/10.1175/MWR-D-16-0253.1.

Mauritsen, T., Svensson, G., Zilitinkevich, S.S., Esau, I., Enger, L. and Grisogono, B. (2007) A total turbulent energy closure model for neutrally and stably stratified atmospheric boundary layers. *Journal of the Atmospheric Sciences*, 64(11), 4113–4126. https://doi.org/10.1175/2007JAS2294.1.

Mogensen, K.S., Magnusson, L. and Bidlot, J.R. (2017) Tropical cyclone sensitivity to ocean coupling in the ECMWF coupled model. *Journal of Geophysical Research: Oceans*, 122(5), 4392–4412. https://doi.org/10.1002/2017JC012753.

Molinari, J., Frank, J. and Vollaro, D. (2013) Convective bursts, downdraft cooling, and boundary layer recovery in a sheared tropical storm. *Monthly Weather Review*, 141(3), 1048–1060. https://doi.org/10.1175/MWR-D-12-00135.1.

Montgomery, M.T. and Smith, R.K. (2014) Paradigms for tropical cyclone intensification. *Australian Meteorological and Oceanographic Journal*, 64(1), 37–66. https://doi.org/10.22499/2.6401.005.

Montgomery, M.T. and Smith, R.K. (2017) Recent developments in the fluid dynamics of tropical cyclones. *Annual Review of Fluid Mechanics*, 49(1), 541–574. https://doi.org/10.1146/annurev-fluid-010816-060022.

Nguyen, C.M., Smith, R.K., Zhu, H. and Ulrich, W. (2002) A minimal axisymmetric hurricane model. *Quarterly Journal of the Royal Meteorological Society*, 128(586), 2641–2661. https://doi.org/10.1256/qj.01.156.

Ooyama, K. (1969) Numerical simulation of the life cycle of tropical cyclones. *Journal of the Atmospheric Sciences*, 26(1), 3–40. https://doi.org/10.1175/1520-0469(1969)026<0003:NSOTLC>2.0.CO;2.

Ooyama, K.V. (1982) Conceptual evolution of the theory and modeling of the tropical cyclone. *Journal of the Meteorological Society of Japan. Series II*, 60(1), 369–380. https://doi.org/10.2151/jmsj1965.60.1_369.

Persing, J., Montgomery, M.T., McWilliams, J.C. and Smith, R.K. (2013) Asymmetric and axisymmetric dynamics of tropical cyclones. *Atmospheric Chemistry and Physics*, 13(24), 12 299–12 341. https://doi.org/10.5194/acp-13-12299-2013.

Pithan, F., Angevine, W. and Mauritsen, T. (2015) Improving a global model from the boundary layer: total turbulent energy

and the neutral limit Prandtl number. *Journal of Advances in Modeling Earth Systems*, 7(2), 791–805. https://doi.org/10.1002/2014MS000382.

Price, J.F. (1981) Upper ocean response to a hurricane. *Journal of Physical Oceanography*, 11(2), 153–175. https://doi.org/10.1175/1520-0485(1981)011<0153:UORTAH>2.0.CO;2.

Pun, I.F., Lin, I.I., Lien, C.C. and Wu, C.C. (2018) Influence of the size of supertyphoon Megi (2010) on SST cooling. *Monthly Weather Review*, 146(3), 661–677. https://doi.org/10.1175/MWR-D-17-0044.1.

Riemer, M., Montgomery, M.T. and Nicholls, M.E. (2010) A new paradigm for intensity modification of tropical cyclones: thermodynamic impact of vertical wind shear on the inflow layer. *Atmospheric Chemistry and Physics*, 10(7), 3163–3188. https://doi.org/10.5194/acp-10-3163-2010.

Rotunno, R., Chen, Y., Wang, W., Davis, C., Dudhia, J. and Holland, G.J. (2009) Large-eddy simulation of an idealized tropical cyclone. *Bulletin of the American Meteorological Society*, 90(12), 1783–1788. http://www.jstor.org/stable/26225163.

Schade, L.R. and Emanuel, K.A. (1999) The ocean's effect on the intensity of tropical cyclones: results from a simple coupled atmosphere–ocean model. *Journal of the Atmospheric Sciences*, 56(4), 642–651. https://doi.org/10.1175/1520-0469(1999)056<0642:TOSEOT>2.0.CO;2.

Schmidt, C.W. and Smith, R.K. (2016) Tropical cyclone evolution in a minimal axisymmetric model revisited. *Quarterly Journal of the Royal Meteorological Society*, 142(696), 1505–1516. https://doi.org/10.1002/qj.2753.

Smith, R.K. (1968) The surface boundary layer of a hurricane. *Tellus*, 20(3), 473–484. https://doi.org/10.1111/j.2153-3490.1968.tb00388.x.

Smith, R.K. (2003) A simple model of the hurricane boundary layer. *Quarterly Journal of the Royal Meteorological Society*, 129(589), 1007–1027. https://doi.org/10.1256/qj.01.197.

Smith, R.K. and Montgomery, M.T. (2015) Toward clarity on understanding tropical cyclone intensification. *Journal of the Atmospheric Sciences*, 72(8), 3020–3031. https://doi.org/10.1175/JAS-D-15-0017.1.

Smith, R.K. and Montgomery, M.T. (2016) The efficiency of diabatic heating and tropical cyclone intensification. *Quarterly Journal of the Royal Meteorological Society*, 142(698), 2081–2086. https://doi.org/10.1002/qj.2804.

Smith, R.K., Montgomery, M.T. and Nguyen, V.S. (2009) Tropical cyclone spin-up revisited. *Quarterly Journal of the Royal Meteorological Society*, 135(642), 1321–1335. https://doi.org/10.1002/qj.428.

Smith, R.K. and Thomsen, G.L. (2010) Dependence of tropical-cyclone intensification on the boundary-layer representation in a numerical model. *Quarterly Journal of the Royal Meteorological Society*, 136(652), 1671–1685. https://doi.org/10.1002/qj.687.

Smith, R.K. and Wang, S. (2018) Axisymmetric balance dynamics of tropical cyclone intensification: Diabatic heating versus surface friction. *Quarterly Journal of the Royal Meteorological Society*, 144(716), 2350–2357. https://doi.org/10.1002/qj.3389.

Tao, W., Shi, J., Chen, S., Lang, S., Lin, P., Hong, S.Y., Peters-Lidard, C. and Hou, A. (2011) The impact of microphysical schemes on hurricane intensity and track. *Asia–Pacific Journal of Atmospheric Sciences*, 47, 1–16.

Vogl, S. and Smith, R.K. (2009) Limitations of a linear model for the hurricane boundary layer. *Quarterly Journal of the Royal Meteorological Society*, 135(641), 839–850. https://doi.org/10.1002/qj.390.

Wadler, J.B., Zhang, J.A., Jaimes, B. and Shay, L.K. (2018) Downdrafts and the evolution of boundary-layer thermodynamics in hurricane Earl (2010) before and during rapid intensification. *Monthly Weather Review*, 146(11), 3545–3565. https://doi.org/10.1175/MWR-D-18-0090.1.

Wang, Y. (2002) An explicit simulation of tropical cyclones with a triply nested movable mesh primitive equation model: TCM3. Part II: model refinements and sensitivity to cloud microphysics parameterization. *Monthly Weather Review*, 130(12), 3022–3036. https://doi.org/10.1175/1520-0493(2002)130<3022:AESOTC>2.0.CO;2.

Wong, M.L. and Chan, J.C. (2004) Tropical cyclone intensity in vertical wind shear. *Journal of the Atmospheric Sciences*, 61(15), 1859–1876.

Wu, C.C., Lee, C.Y. and Lin, I.I. (2007) The effect of the ocean eddy on tropical cyclone intensity. *Journal of the Atmospheric Sciences*, 64(10), 3562–3578. https://doi.org/10.1175/JAS4051.1.

Yablonsky, R.M. and Ginis, I. (2012) Impact of a warm ocean eddy's circulation on hurricane-induced sea-surface cooling with implications for hurricane intensity. *Monthly Weather Review*, 141(3), 997–1021. https://doi.org/10.1175/MWR-D-12-00248.1.

Yan, Y., Li, L. and Wang, C. (2017) The effects of oceanic barrier layer on the upper ocean response to tropical cyclones. *Journal of Geophysical Research: Oceans*, 122(6), 4829–4844. https://doi.org/10.1002/2017JC012694.

Zängl, G., Reinert, D., Rípodas, P. and Baldauf, M. (2015) The ICON (ICOsahedral Non-hydrostatic) modelling framework of DWD and MPI-M: description of the nonhydrostatic dynamical core. *Quarterly Journal of the Royal Meteorological Society*, 141(687), 563–579. https://doi.org/10.1002/qj.2378.

Zhang, D.L., Liu, Y. and Yau, M.K. (2001) A multiscale numerical study of Hurricane Andrew (1992). Part IV: unbalanced flows. *Monthly Weather Review*, 129(1), 92–107. https://doi.org/10.1175/1520-0493(2001)129<0092:AMNSOH>2.0.CO;2.

Zhang, J.A., Cione, J.J., Kalina, E.A., Uhlhorn, E.W., Hock, T. and Smith, J.A. (2017) Observations of infrared sea surface temperature and air–sea interaction in hurricane Edouard (2014) using GPS dropsondes. *Journal of Atmospheric and Oceanic Technology*, 34(6), 1333–1349. https://doi.org/10.1175/JTECH-D-16-0211.1.

Zhang, J.A. and Marks, F.D. (2015) Effects of horizontal diffusion on tropical cyclone intensity change and structure in idealized three-dimensional numerical simulations. *Monthly Weather Review*, 143(10), 3981–3995. https://doi.org/10.1175/MWR-D-14-00341.1.

Zhang, J.A., Marks, F.D., Montgomery, M.T. and Lorsolo, S. (2010) An estimation of turbulent characteristics in the low-level region of intense Hurricanes Allen (1980) and Hugo (1989). *Monthly Weather Review*, 139(5), 1447–1462. https://doi.org/10.1175/2010MWR3435.1.

Zhang, J.A., Rogers, R.F., Nolan, D.S. and Marks, F.D. (2011) On the characteristic height scales of the hurricane boundary layer. *Monthly Weather Review*, 139(8), 2523–2535. https://doi.org/10.1175/MWR-D-10-05017.1.

Zhu, T. and Zhang, D.L. (2006) Numerical simulation of Hurricane Bonnie (1998). Part II: sensitivity to varying cloud microphysical processes. *Journal of the Atmospheric Sciences*, 63(1), 109–126. https://doi.org/10.1175/JAS3599.1.

APPENDIX A. SLAB BOUNDARY-LAYER MODEL

The equations in the slab boundary layer are solved for the radial velocity, $u_b(r)$, tangential velocity, $v_b(r)$, and vertical velocity, $w_h(r)$. Since the equations are steady state, the equations are solved separately for each time step. That is, a unique $u_b(r)$, $v_b(r)$, and $w_h(r)$ are obtained for each time step. Assuming that $u_b(r)$ and $v_b(r)$ are in geostrophic balance (not gradient wind balance) at a large radius, $r = R$, allows the equations to be solved for $u_b(R)$ and $v_b(R)$. The complete solutions to these equations are then obtained by incrementally integrating $u_b(r)$ and $v_b(r)$ radially inwards. As an intermediate step between each integration, the vertical velocity, $w_h(r)$, is computed with the local values of $u_b(r)$ and $v_b(r)$.

The equations are formulated on an f-plane in cylindrical polar coordinates and are given by

$$\frac{du_b}{dr} = \frac{w_{h-}}{h} - \frac{(v_g^2 - v_b^2)}{ru_b} - \frac{f(v_g - v_b)}{u_b} - \frac{C_D}{h}(u_b^2 + v_b^2)^{1/2}, \tag{A1}$$

$$\frac{dv_b}{dr} = \frac{w_{h-}}{h}\frac{(v_b - v_g)}{u_b} - \left(\frac{v_b}{r} + f\right) - \frac{C_D}{h}(u_b^2 + v_b^2)^{1/2}\frac{v_b}{u_b}, \tag{A2}$$

$$w_h = \frac{h}{1+\alpha}\left[\frac{1}{u_b}\left\{\frac{v_g^2 - v_b^2}{r} + f(v_g - v_b) + \frac{C_D}{h}(u_b^2 + v_b^2)^{1/2}\right\} - \frac{u_b}{r}\right]. \tag{A3}$$

The slab boundary-layer model treats the boundary layer as a single slab with no variation in the vertical, so that u_b and v_b are functions of radius only. Multiplying Equation A1 by u_b gives the radial momentum equation. Similarly, multiplying Equation A2 by u_b returns the tangential momentum equation. The terms on the left-hand side of Equations A1 and A2 correspond to the radial advection of radial momentum and tangential momentum, respectively. The first terms on the right-hand side of these equations relate to the vertical advection of momentum. The term w_{h-} is related to w_h by $w_{h-} = \frac{1}{2}(w_h - |w_h|)$. For the case of negative w_h, w_{h-} and w_h have the same magnitude. If w_h is positive, w_{h-} is zero. Physically, this means that only downward advection of momentum from above the boundary layer influences the dynamics in the boundary layer, and not the upward advection of momentum out of the boundary layer. The second and third terms on the right-hand side in Equation A1 are equivalent to the agradient force per unit mass divided by u_b. Here, v_g and f are the gradient wind above the boundary layer and the Coriolis parameter, respectively. The agradient force per unit mass, given by $(v_g^2 - v_b^2)/r + f(v_g - v_b)$, is the sum of the Coriolis and centrifugal forces for v_g minus the sum of Coriolis and centrifugal forces for v_b. The agradient force represents the radial force imbalance between the radial pressure gradient in the slab boundary layer, which is given by the sum of Coriolis and centrifugal forces for v_g, and the Coriolis and centrifugal forces in the slab boundary layer. When the agradient force is zero, the flow is in gradient wind balance. Hence, the agradient force quantifies the deviation of the flow from gradient wind balance. Finally, the last term in Equations A1 and A2 represents the effect of friction at the surface, which depends on the drag coefficient, C_D, and the horizontal wind speed, $(u_b^2 + v_b^2)^{1/2}$. For further information on this boundary-layer model, the reader is referred to Smith (2003).